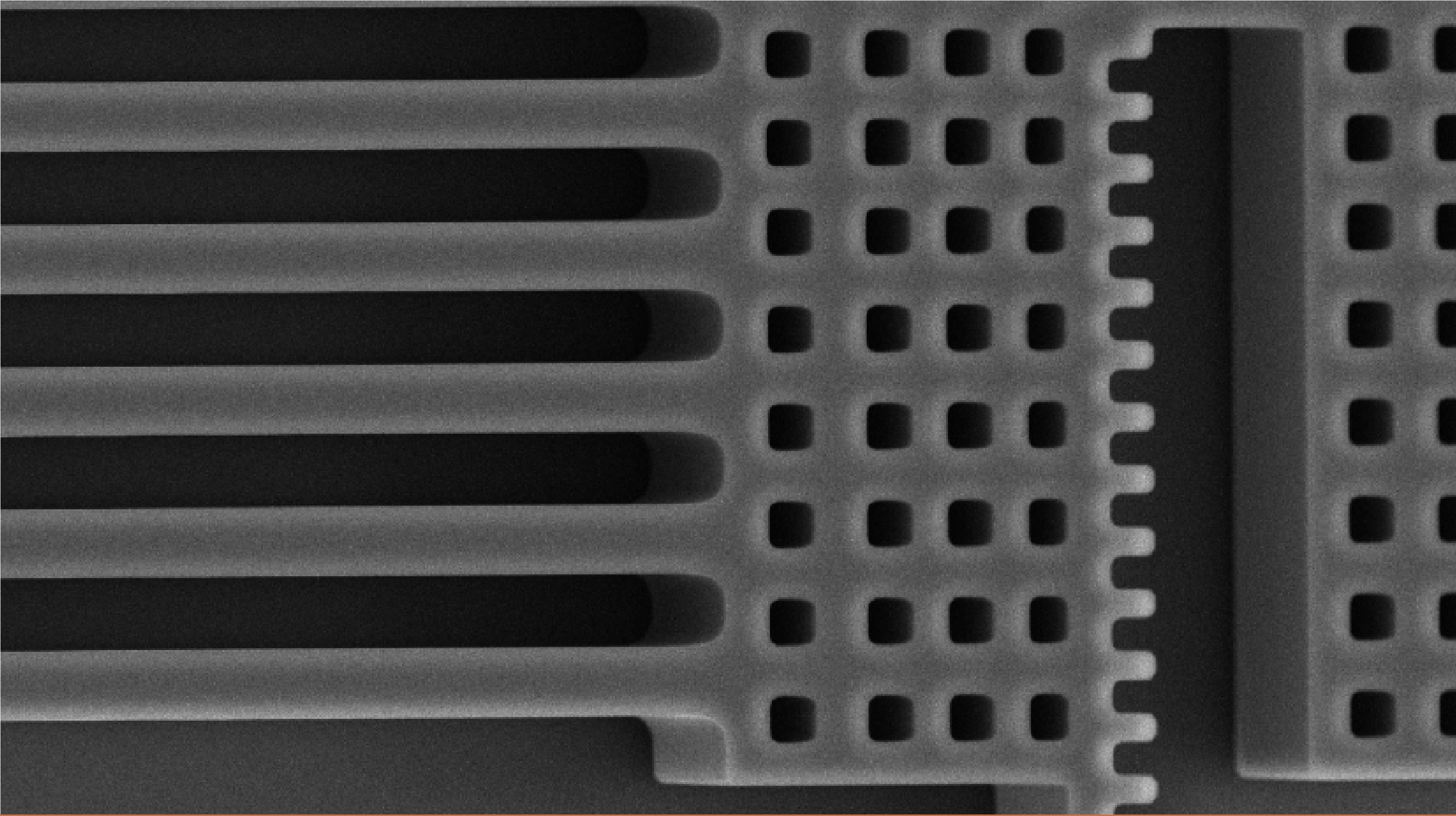

Towards a High Dynamic Range Resonant MEMS Accelerometer

Master Thesis Electrical Engineering

B.A. Boom

Supervising Committee

Prof. dr. ir. J.C. Lötters | dr. ir. R.J. Wiegerink
dr. ir. N.R. Tas | dr. ir. A.J. Annema

August 2015

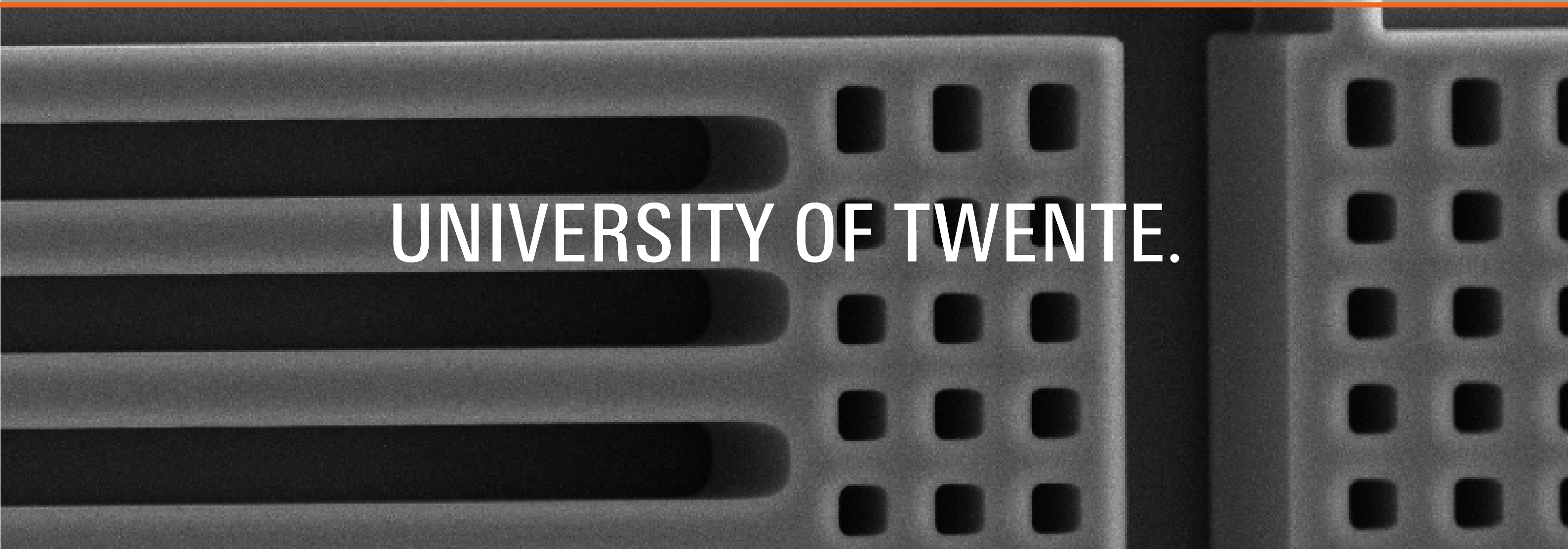

UNIVERSITY OF TWENTE.

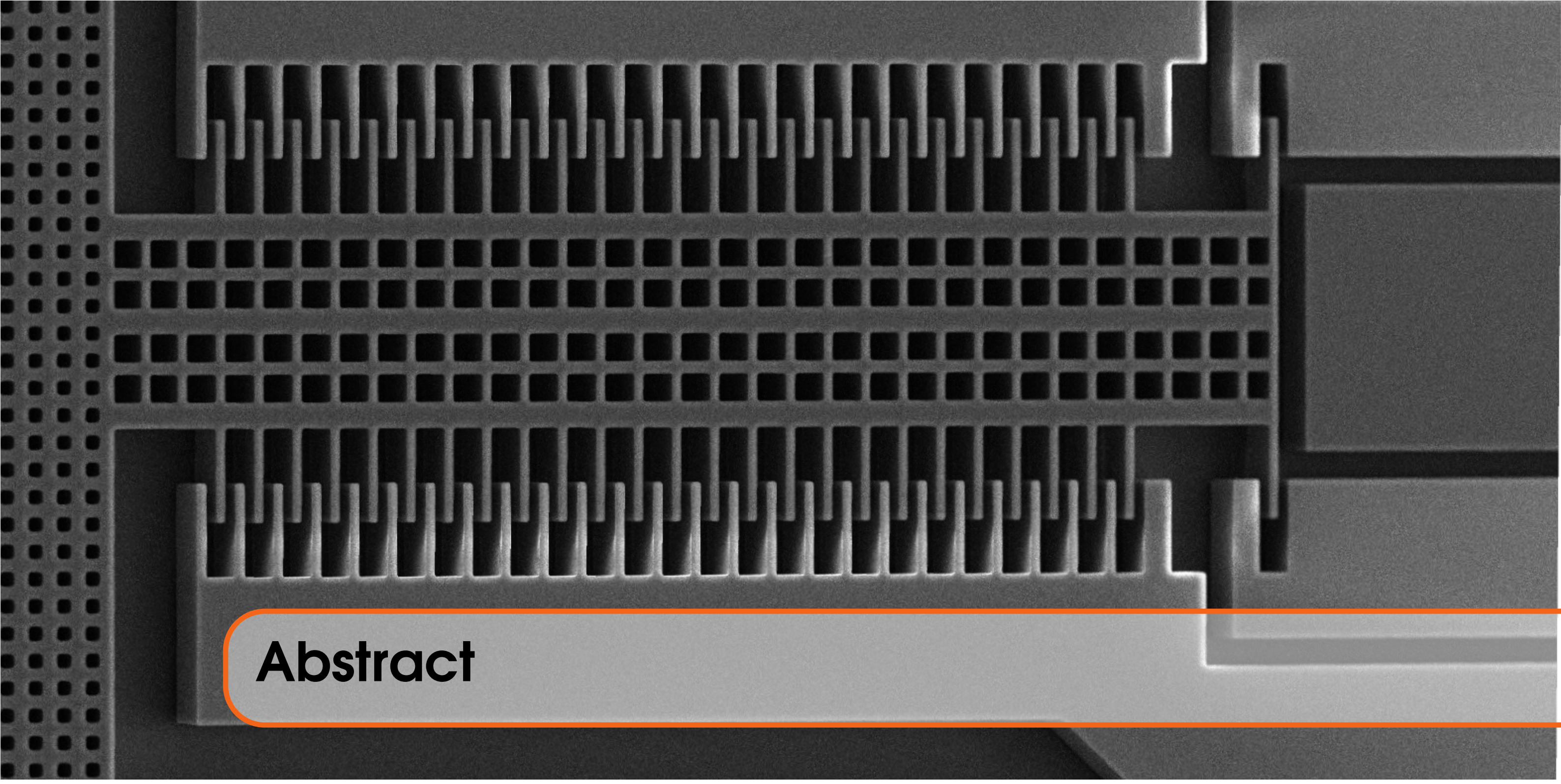

Abstract

This work is focused around the double ended tuning fork transducer. This transducer structure changes its resonance frequency when a load is applied to it. This change in resonance frequency can be very accurately measured, providing a high dynamic range.

A MEMS device was designed to characterize the tuning fork behavior as a function of different external parameters, such as axial loads, readout electronics and pressure. Depending on the pressure, the tuning fork quality factor can be made very high, up to about 100.000. This is comparable to the highest quality factors reported for similar structures. A reliable way was established to measure the mechanical quality factor through an electronic interface, without the need to perform a ringdown measurement. This method can be useful for other high quality factor systems as well.

Measured tuning fork sensitivities vary between $1-3MHz/N$, depending on the applied axial load. This corresponds very well to the model that has been derived to describe the behavior of the tuning fork as a function of external parameters. The transducer sensitivity is found to increase with a compressive axial load. Increases up to a factor 3 are observed relative to the sensitivity of an unloaded tuning fork.

The electronic readout has a large influence on both the resonance frequency of the tuning fork, and its stability. Any noise in the power supply couples directly to the resonance frequency, which severely limits the sensing resolution. This coupling is modeled and investigated experimentally. Moreover, a measurement scheme was developed to remove the influence of the readout electronics from the results. Using this scheme, purely mechanical parameters can be extracted.

The nonlinear limits of a tuning fork in operation are investigated. Interesting effects can be seen here, as these limits can be stretched by tuning nonlinearities of different origin in such a way that they cancel. Measurement results indicate that it could be possible to get rid of all nonlinear effects up to the second order. This is beneficial for the transducer's signal to noise ratio, as removing nonlinearities means that it can be driven at higher amplitudes.

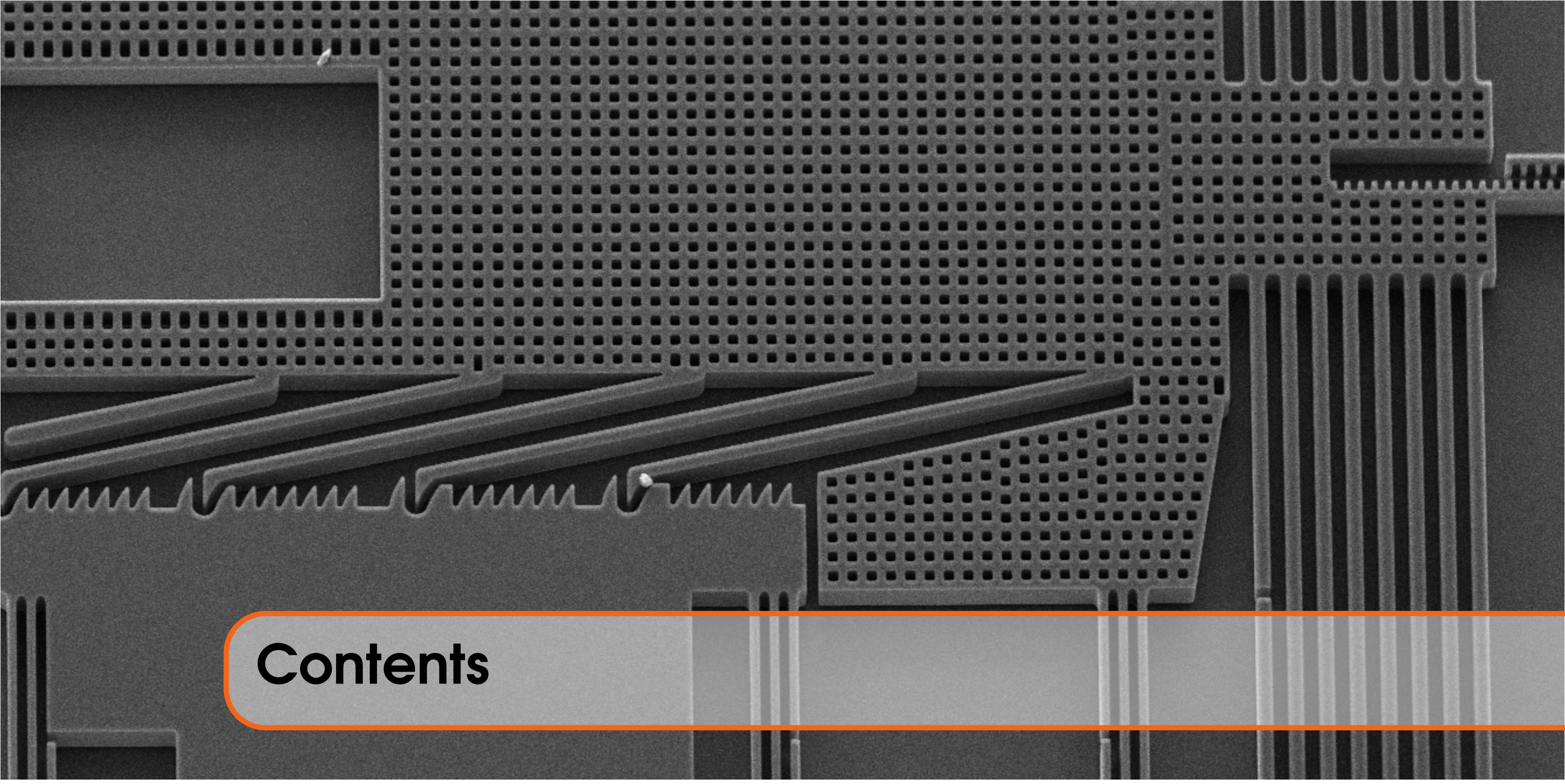

Contents

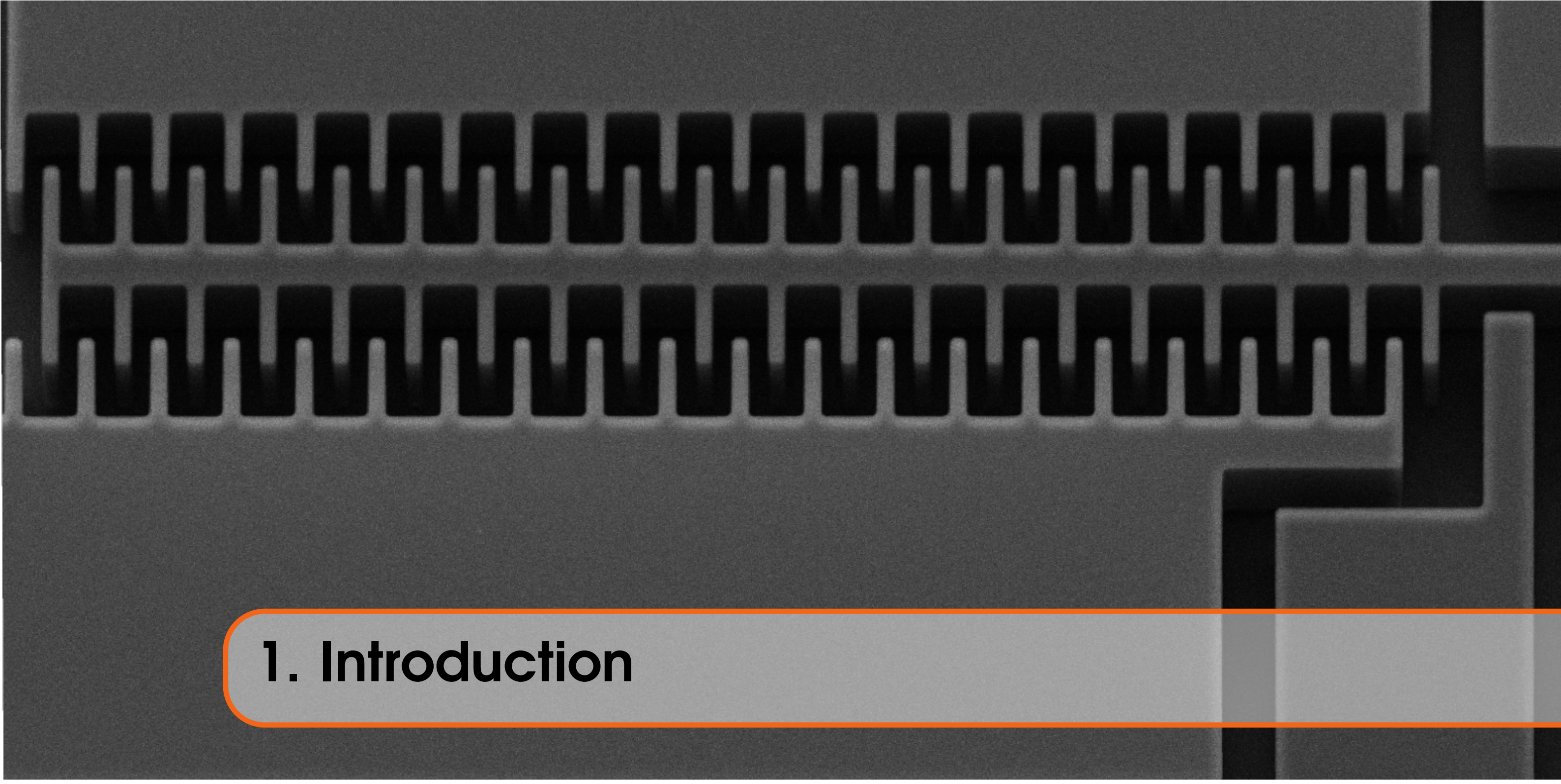

1. Introduction

The VIRGO detector in Italy was built over a decade ago to allow for observation of gravitational waves. It is a giant Michelson interferometer with arms that are 3 kilometers long each. The optical components in the system should remain perfectly still in order to be able to observe passing gravitational waves. To shield the mirrors from ground motion, large seismic attenuation towers were constructed that suppress seismic motion by a factor of $\sim 10^{12}$ [1]. However, seismic motion around the interferometer does not only impose a motion on the seismic attenuators, it also modulates the distribution of mass around the interferometer mirrors. These mass distribution modulations cause small fluctuations in the gravity on the mirrors, so-called Newtonian noise. Newtonian noise on the mirrors cannot be shielded by the seismic attenuators and poses a lower limit on the position stability of the mirrors. The seismic attenuators are so good, that the dominant source for residual mirror motion is this Newtonian noise. To improve the sensitivity of the VIRGO setup, effort is made to upgrade it to Advanced VIRGO [2]. One of the points to be addressed there is the effect of Newtonian noise.

Newtonian noise cannot be directly shielded, but by accurately monitoring seismic activity on the VIRGO site, effects of Newtonian noise can be subtracted from the measurement data. This application calls for highly sensitive seismic sensors, that can be easily deployed around the optical components of VIRGO. Per optical site, a few thousand sensors with a noise floor around $1ng/\sqrt{Hz}$ are needed to reach the desired accuracy [4]. Because so many sensors are needed, they should be easily producible in bulk. This is why a project was started to develop a MEMS sensor that is sensitive enough for this application. Once such a sensor is shown to be sensitive enough, it can be relatively easily produced in bulk quantities.

A very sensitive MEMS accelerometer was developed in collaboration with the Nikhef institute that makes use of geometric antispring technology. By compressing a set of springs, the resonance frequency of the proofmass can be made very low, and therefore the sensitivity and self noise level become very good. This sensor reaches the desired noise floor of $1ng/\sqrt{Hz}$ under proper vacuum conditions, but its full scale range is not sufficient for use in the vertical dimension. Measuring small gravity fluctuations in this direction is very difficult, because there is always a very large offset present. This calls either for mechanical solutions that will compensate the offset, or for a readout mechanism with an extremely high dynamic range. In the last case, using a frequency as a measurand is attractive, because it can be measured very accurately over a large range of values. This work will serve as a first investigation into this field and one of the basic structures that can transform a measured force to a frequency is thoroughly studied.

1.1 State of the Art

MEMS accelerometers have been around since the nineties. Most of them are designed for the consumer market and are currently used by the automotive and consumer industry in airbag deployment sensors, game controllers and smartphones. Only very few sensors exist that are aimed for the more sensitive applications such as seismology. Colibrys sells a commercially available MEMS seismometer that reaches a noise level of $\sim 50ng/\sqrt{Hz}$ between 2 and 1000Hz and Sercel sells modules that can reach $\sim 40ng/\sqrt{Hz}$ in the same band. These sensors use a capacitive feedback Silicon Currently, no commercial device is available that has a self noise around $1ng/\sqrt{Hz}$. [14]

Different research groups around the world are trying to develop MEMS seismometers approaching this $1ng/\sqrt{Hz}$ noise level. A variety of sensing approaches is used to this end. The best design up to now is a bulk micromachined sensor developed by the Optical and Semiconductor Devices Group at Imperial College, London. This design uses a capacitive structure to readout the position and an inductive technique to apply a feedback force. It demonstrated a noise performance of $2-3ng/\sqrt{Hz}$ over $0.04-0.1Hz$ [14]. Unfortunately, the noise becomes higher outside this frequency band.

The seismometer designed by the Nikhef institute uses new geometric antispring technology and has demonstrated noise performance approaching the $1ng/\sqrt{Hz}$ goal. A search for other devices like it reveals that it really is the state of the art at this point. The problem they are facing at the moment is that their structure lacks the full range capabilities to measure accelerations vertically. A resonant readout transducer structure has a large dynamic range and frequencies are relatively easy to measure, so this can be an attractive option. In [3], a dynamic range of $140dB$ was reported using a double ended tuning fork structure. In this work, the double ended tuning fork structure will be studied for applicability in an ultra sensitive accelerometer.

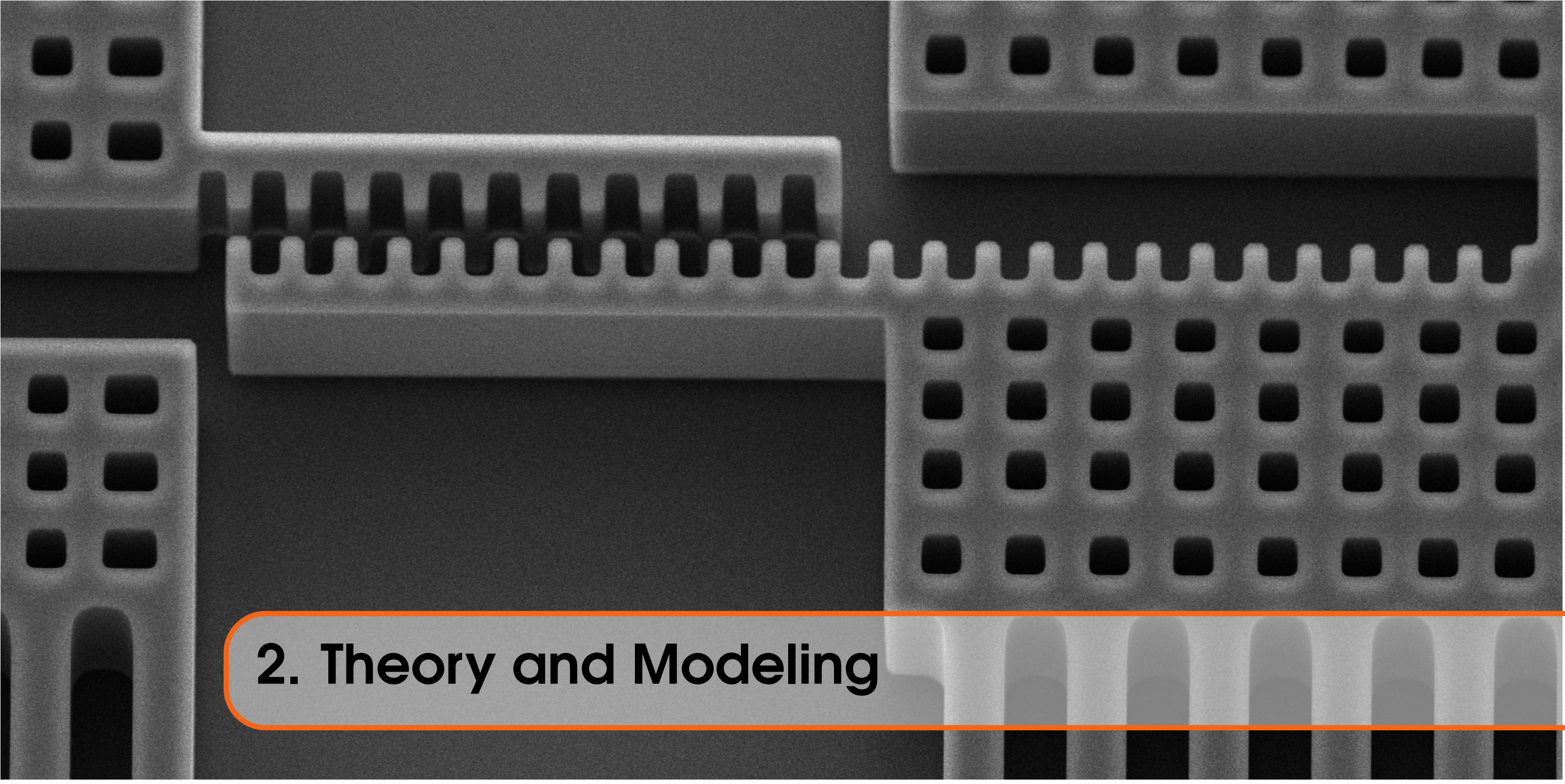

2. Theory and Modeling

This work is focused around the double ended tuning fork transducer, or DETF for short. In figure 2.1, a schematic representation of such a DETF is shown. Effectively, the DETF is a force sensing structure, converting an axial load into a certain shift in resonance frequency.The heart of the DETF is the two long parallel beams in the center, attached to the perforated blocks at the end. Loading these tines with a force F will change the resonance frequency of the total structure. This is the essential function of the DETF, the T-shaped structures attached to the center of the parallel beams are only there to accommodate electrical readout and actuation of the structure. To accurately describe the DETF behavior, an analytical model is needed. In this chapter, an expression for the DETF resonance frequency will be derived incorporating the effects of geometry, axial load and electrical readout. Firstly, however, a closer look is taken at the electrical readout and actuation structure.

2.1 Electrical readout

The resonance frequency of a DETF can only be measured if the structure can be actuated with a certain frequency and the response can be recorded. As is common in MEMS devices, the interfacing to the outside world is done via a capacitive transducer structure. The T-shaped structure

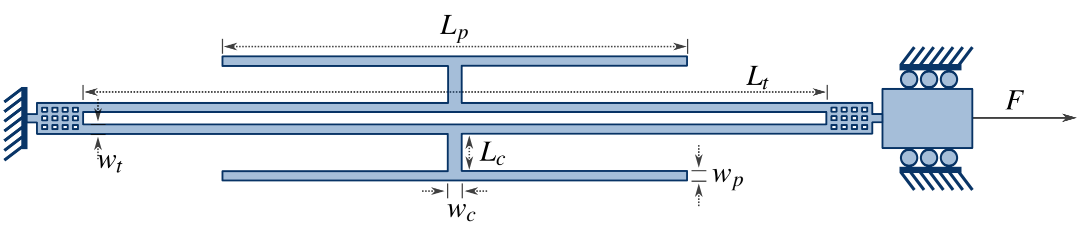

Figure 2.1: Schematic representation of a DETF structure's top view. The structure is fixed on the left side and can be loaded with a force, F, through the roller structure on the right. Variables denoting the relevant dimensions are annotated in the drawing. The structure is made out of a single layer of thickness t.

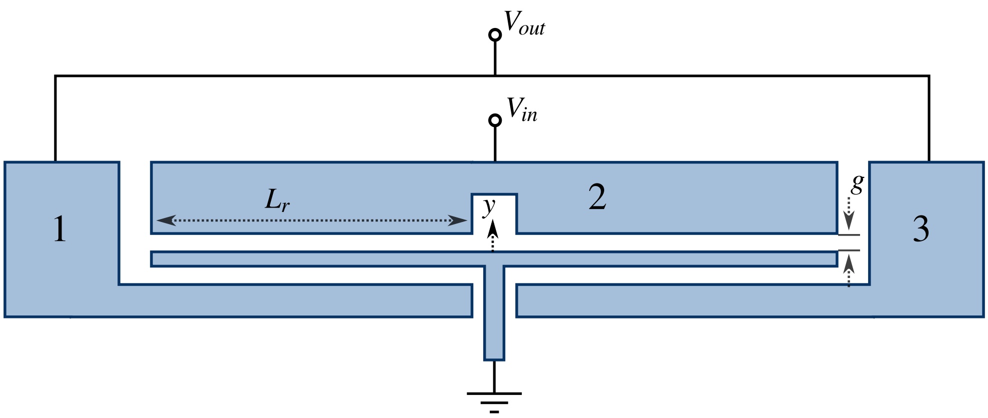

Figure 2.2: A close up of the readout beam from figure 2.1. In this drawing also the surrounding electrodes are shown, forming parallel plate capacitors with the readout beam. Electrodes 1 and 3 are connected and maintained at V_{out}. V_{in} is applied to electrode 2. The rotor can move back and forth in direction y.

that is attached to the center of the DETF tines in figure 2.1 will form parallel plate capacitors with electrodes surrounding the structure. This T-shaped structure will be called the rotor from now on, to distinguish it from the static electrodes, or stators.

The capacitance between the rotor and the stators will change as the rotor moves. This way, the position of the center of the DETF tine can be recorded as a function of time and a readout can be established. The capacitive structures also work the other way. Applying a voltage across the rotor and the stators will generate a force on the rotor. This also provides a way to drive the DETF structure.

In figure 2.2 one of the readout structures is shown. In the center the T-shaped rotor can be recognized and 3 stators are surrounding it. Stators 1 and 3 are electrically connected, so they effectively form only one electrode. The rotor itself is grounded to avoid pull-in effects to the substrate below it [13, Sec. 7.9]. An input voltage is applied on electrode 2 and stators 1 and 3 carry the output voltage. This output will be connected to a charge amplifier later, so the output voltage can assumed to be constant.

To be able to get a signal out of the changing capacitances, they have to be charged. To do this, all stators are biased with the same voltage, V_b. When the rotor moves, the capacitances between the rotor and stator electrodes will change and currents will flow. At the output this current will be measured by a charge amplifier. The output current is given by

$$i_{out} = \frac{\partial (C_{out} V_{out})}{\partial t} = V_b \frac{\partial C_{out}}{\partial t} = V_b \frac{\partial C_{out}}{\partial y} \frac{dy}{dt} = \eta \dot{y} \tag{2.1}$$

where η is the transduction coefficient linking the output current to the velocity of the rotor. Because the readout electrodes are symmetrical and the input is biased at V_b as well, the input current is given by the same transduction coefficient, but with an additional 180° phase shift.

Biasing the stators is useful for obtaining an output signal, but it will also interfere with the resonance frequency of the DETF. This is because effectively, biasing the structure will introduce a negative spring constant and this will lower the resonance frequency. This can be seen through the co-energy, $U'(y)$, stored in the capacitors. This co-energy is simply $U' = -C_{tot}(y)V_b^2/2$ [13, Sec. 7.8]. The spring constant that is introduced can be obtained by differentiating two times:

$$c_{el} = -\frac{\partial F}{\partial y} = \frac{\partial}{\partial y}\left(\frac{\partial U'}{\partial y}\right) = -\frac{V_b^2}{2}\frac{\partial^2 C_{tot}}{\partial y^2}. \tag{2.2}$$

The effect of this electrical spring on the resonance frequency is significant and has to be accounted for in modeling the resonance frequency of the system. In the next section, such a model will be derived.

2.2 Resonance Frequency

Different things will influence the resonance frequency of a DETF. Its geometry is the most straightforward one. Shortening the tines will make them stiffer and therefore the resonance frequency will go up. Enlarging the readout electrodes will increase the mass of the system and will decrease the resonant frequency. The interesting influence in this case is the change in resonance frequency when an axial load is applied. This can be compared to a guitar string, that will vibrate with higher frequency if its tension is increased. In contrast with a guitar string, the DETF also has a defined resonance frequency with no load applied. It can therefore also decrease its frequency when a compressive axial load is applied. The last influence on the resonance frequency is an unwanted one that is introduced by the electronic readout as explained in section 2.1.

In appendix A.2 the concept of Lagrangian dynamics is introduced. This method uses an analysis of a system's internal energy to describe its dynamics. In this appendix, Lagrangian dynamics along with the concept of mode shapes is used to derive an expression for the resonance frequency of an axially unloaded DETF. Using reasoning along the same lines, it is possible to also incorporate the effect of axial loading and the negative spring that is introduced by the electrical readout. It is only necessary to include the extra energy terms that are caused by these effects in the Lagrangian.

For a stationary vibration, the shape of a DETF beam can be described by a function where the variables of time and position are separated. The shape of the beam then takes the form

$$v(x,t) = q(t) \cdot X(x), \tag{2.3}$$

where $q(t)$ is a continuous, periodic function of t and $X(x)$ is the so called mode shape of the vibration. This means that every point on the DETF beam performs the same periodic motion $q(t)$ with an amplitude that is dependent on the position and is described by $X(x)$. Determining the exact mode shape of vibration for the DETF structure as shown in figure 2.1 is hard, but it can be approximated by different functions. An analysis of the accuracy of different mode shape functions is done in appendix A.2.2 and A.2.4. The result of this analysis is that using the static deflection function of a prismatic beam with a load at its center will give the most accurate results. The prediction for the resonance frequency will be accurate to well within 1.7%. The functional form of the mode shape that will be used for further modeling will therefore be given as in equation 2.4. The mode shape described by this function is illustrated in appendix A.2.2.

$$X(x) = \begin{cases} 12\left(\frac{x}{L_t}\right)^2 - 16\left(\frac{x}{L_t}\right)^3 & 0 < x \le L_t/2 \\ 12\left(1-\frac{x}{L_t}\right)^2 - 16\left(1-\frac{x}{L_t}\right)^3 & L_t/2 < x < L_t \end{cases} \tag{2.4}$$

Following the lines of appendix A.2 the different energy terms in the system can be obtained from this mode shape. From the appendix, the kinetic energy, T, and the potential energy originating from the bending of the beam, U_{bend}, are already known:

$$U_{bend} = \frac{EI}{2} q(t)^2 \cdot C_1 \quad \text{with} \quad C_1 = \int_0^{L_t} \left(\frac{\partial^2 X(x)}{\partial x^2}\right)^2 dx \tag{2.5}$$

$$T = \frac{1}{2}\dot{q}(t)^2 \cdot C_2 \quad \text{with} \quad C_2 = \rho t w_t \int_0^{L_t} X(x)^2 dx + m_c X(L/2)^2, \tag{2.6}$$

where E is the DETF tine Young's modulus, I is its area moment of inertia, ρ is the DETF material density, t is the device layer thickness and m_c is the mass of the readout electrode.

In this case, there are two other effects that have to be included in the Lagrangian. The bias voltage on the readout electrodes and an axial load both introduce an extra energy term. The energy stored in the capacitive readout system is given by $U'_{el} = -C(x)V_b^2/2$ [13, Sec. 7.8]. Using the parallel plate approximation for the capacitance of the readout structure gives

$$C_{tot} = 2L_r t\varepsilon_0 \left(\frac{1}{g-y} + \frac{1}{g+y}\right) \approx \frac{4L_r t\varepsilon_0}{g}\left(1 + \frac{y^2}{g^2}\right). \tag{2.7}$$

Now y is given by $X(L/2)q(t) = q(t)$, so the additional potential energy term introduced by biasing the electrodes is given by

$$\Delta U_{el} = -\left(\frac{C_{tot}(q(t))V_b^2}{2} - \frac{C_{tot}(0)V_b^2}{2}\right) = -\frac{2L_r t\varepsilon_0 V_b^2}{g^3}\cdot q(t)^2 = -\frac{1}{2}C_3 \cdot q(t)^2, \tag{2.8}$$
$$\text{with} \quad C_3 = \frac{4L_r t\varepsilon_0 V_b^2}{g^3}.$$

The last energy term to be considered originates from the axial load. When the DETF beam deflects, the total length of the beam slightly increases and the potential energy that is stored in the compression will increase [18, p. 364]. The length increase of the beam can be written as

$$\delta L = \int_0^{L_t} ds - dx = \int_0^{L_t} \left(\sqrt{\left(\frac{\partial X(x)q(t)}{\partial x}\right)^2 + 1} - 1\right) dx \approx \frac{1}{2}q(t)^2 \int_0^{L_t} \left(\frac{\partial X(x)}{\partial x}\right)^2 dx, \tag{2.9}$$

where ds is an infinitesimally small length along the mode shape curve $X(x)$. An axial force that is applied to a beam that is changing length is doing some work. Noting that the force applied to one tine is equal to half the force on the DETF, the work done by the force can be written as

$$U_{ax} = \frac{F}{4}q(t)^2 \int_0^{L_t} \left(\frac{\partial X(x)}{\partial x}\right)^2 dx = \frac{12F}{10L_t}q(t)^2 = \frac{1}{2}C_4 \cdot q(t)^2 \tag{2.10}$$
$$\text{with} \quad C_4 = \frac{12F}{5L_t},$$

where F is the tensile axial force on the DETF structure and the integral is evaluated with the mode shape $X(x)$ as in equation 2.4.

The results in equations 2.5, 2.6, 2.8 and 2.10 describe all internal energy terms in the system. Using these energies, the Lagrangian of the system is given by

$$\mathscr{L} = T - U = \frac{1}{2}\cdot C_2 \cdot \dot{q}(t)^2 - \frac{1}{2}(EI \cdot C_1 - C_3 + C_4)\cdot q(t)^2. \tag{2.11}$$

This Lagrangian is perfectly equivalent to that in appendix A.2.3 and the solution to the differential equation will therefore be the same, be it with different constants C_n. The resonance frequency that follows from this solution is shown in relation 2.1. In [3] a model was derived for a similar DETF structure. The two models correspond very well, with the exception of a factor of 2 in the electric spring term. In [3], only the input part of the readout capacitance is considered in the model, while also the output carries a regulated voltage. The output therefore also introduces an electric spring and the influence of the readout structure is twice as large as stated there.

Relation 2.1 in itself is not very insightful, therefore the model is plotted in figure 2.3. The unloaded resonance frequency is denoted by ω_0. When a tensile load (positive) is applied, the resonance frequency increases. It will keep increasing until at some point, the DETF will break.

Relation 2.1 — DETF loaded resonance frequency. The resonance frequency of a DETF with dimensions as shown in figures 2.1 and 2.2, loaded by an axial force, F, and with a bias V_b on the readout electrodes, is given by

$$\omega_0 = \sqrt{\frac{EI \cdot C_1 - C_3 + C_4}{C_2}} = \sqrt{\frac{\frac{192EI}{L_t^3} - \frac{4L_r t \varepsilon_0}{g^3} \cdot V_b^2 + \frac{12}{5L_t} \cdot F}{\frac{13}{35}\rho L_t w_t t + m_c}} \tag{2.12}$$

$$\text{with} \quad I = \frac{w_t^3 t}{12}. \tag{2.13}$$

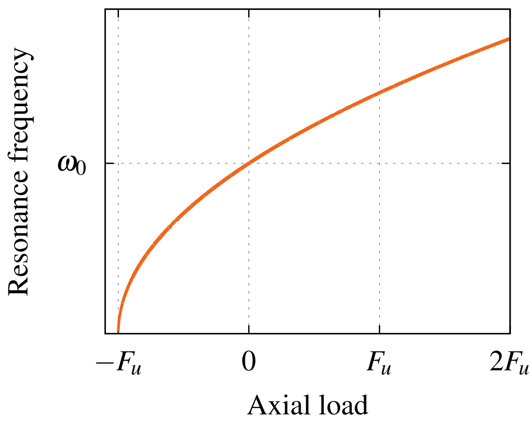

Figure 2.3: DETF resonance frequency as a function of axial load. ω_0 denotes the unloaded resonance frequency and $F_u = 80EI/L_t^2$ is the force at which the system becomes unstable.

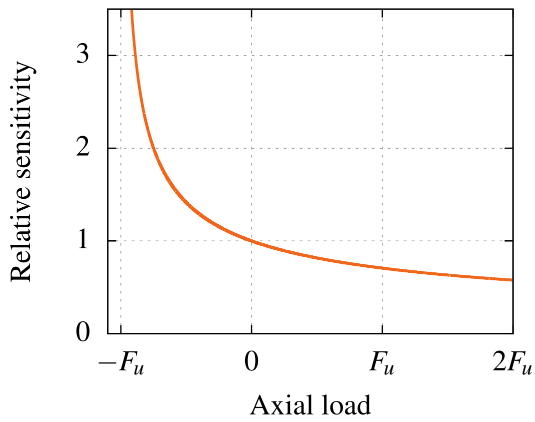

Figure 2.4: Relative sensitivity to small loads as a function of axial load. Sensitivities are normalized to the unloaded sensitivity.

When a compressive load (negative) is applied, the resonance frequency decreases to zero when a certain load is applied. The load at which this happens is predicted by the model as $F_u = 80EI/L_t^2$, which is close to the classical buckling load $8\pi^2 EI/L_t^2$ [15, p. 106].

The slope of the curve in figure 2.3 represents the DETF sensitivity to small changes in the axial load. For tensile axial loads the DETF sensitivity decreases and with compressive loads, it increases with respect to the unloaded sensitivity. This change in sensitivity is shown in figure 2.4. For compressive loads close to F_u, the DETF sensitivity increases rapidly. The relative sensitivity is 2 for $F = 3/4 \cdot F_u$ and 3 for $F = 8/9 \cdot F_u$. This increase in sensitivity could be beneficial for use in a very sensitive vertical accelerometer. By designing the structure in a way that the proofmass is suspended by the DETF structure, the weight of the proofmass could be chosen as $3/4 \cdot F_u$, gaining a factor of 2 in sensitivity to small accelerations. This way the 1g offset in this direction that is considered a disadvantage can also be used to benefit the sensor. Theoretically, the sensitivity can be increased indefinitely, by choosing an operating point close to F_u. In reality however, the structure will likely buckle somewhat before reaching a load of F_u. How large the sensitivity increase can be in practice will be investigated further.

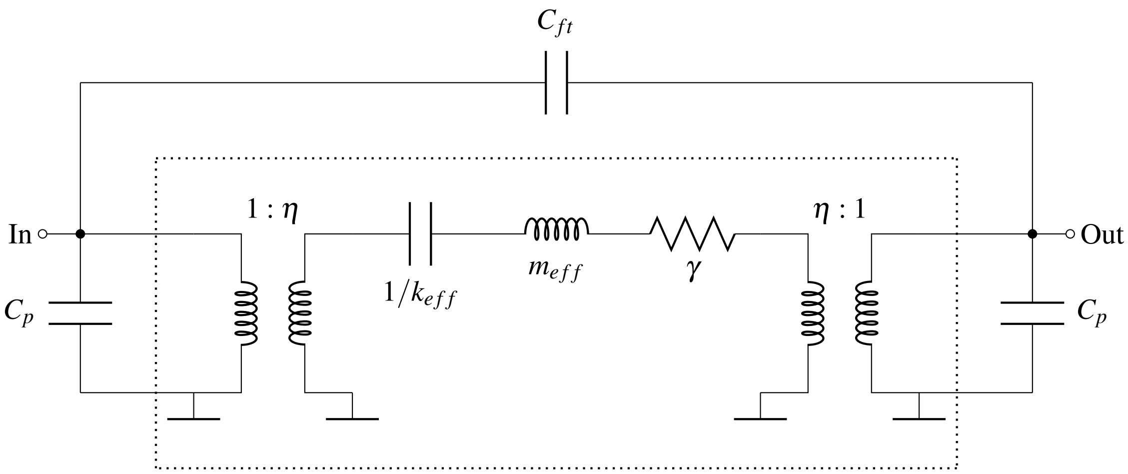

Figure 2.5: Electrical equivalent model of the DETF. The part inside the dashed box represents the mechanical domain. The nodes indicated with 'In' and 'Out' can be considered to be the points where the MEMS structure can be connected to the measurement electronics. Parasitics are indicated as well.

2.3 Electrical model

The dependence of the DETF resonance frequency on all kinds of external parameters as derived in section 2.2 is quite complicated. However, once the external parameters are fixed, the resonance frequency is defined and the entire system can be described by a simple second order model with an effective mass, an effective spring constant and a damping constant. As is often done with such mechanical MEMS systems, a parallel can be made with the electrical domain to allow for analysis in a circuit simulator. The differential equation representing the mechanical system is given by

$$m_{eff}\cdot\ddot{y}+\gamma\cdot\dot{y}+c_{eff}\cdot y=f(t), \tag{2.14}$$

where m_{eff}, γ, c_{eff} and $f(t)$ are the effective mass, damping constant, effective spring constant and driving force respectively. This differential equation is perfectly equivalent to that of a driven LCR tank with an inductor of value m_{eff}, a capacitor of value $1/c_{eff}$ and a resistor of value γ. The driving force already is of electrical nature and is originates from a small AC driving signal added to the large bias on the input electrode. The total force resulting from the input electrode then is

$$F(t)=\frac{\partial}{\partial y}\left(\frac{1}{2}C_{in}(y)\cdot V^2\right)=\frac{1}{2}\frac{\partial C_{in}(y)}{\partial y}(V_b+v_{drive})^2\approx\frac{1}{2}\frac{\partial C_{in}(y)}{\partial y}\cdot V_b^2+\eta v_{drive}, \tag{2.15}$$

which consists of a DC term and a small AC term. Because the output electrode is biased at the same voltage, it exerts exactly the same DC force in the opposite direction, such that the driving force is given by only an AC term, $f(t)=\eta v_{drive}$. Schematically, this mechanical system can be represented as the two port circuit shown in the dashed box in figure 2.5. The transformers couple the electrical domain to the mechanical domain as stated in equation 2.1.

The terminals 'In' an 'Out' can be physically connected to measurement electronics. These terminals also introduce parasitics in the system. The parasitics to ground, C_p, are not much of a problem at the signal frequencies of interest, but there is also a direct feedthrough capacitance between the input and output terminal, C_{ft}. This parasitic capacitance does give some problems as it introduces an additional phase shift close to the DETF resonance. As an example, a typical unloaded DETF from this work will be considered. As will be seen later, such a DETF has an effective mass of about $0.7ng$, an effective spring constant of $67N/m$ and a quality factor of about 100.000 ($\gamma\approx 2.1\cdot 10^{-9}Ns/m$). Simulating such a structure in a circuit simulator with a feedthrough capacitance of $1pF$ gives the transfer as shown in figure 2.6. Sweeping from left to right, the

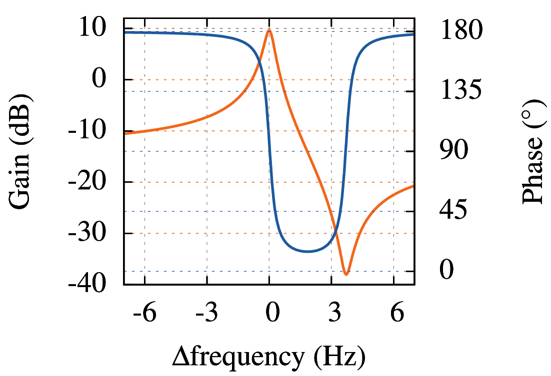

Figure 2.6: Simulation of a DETF with a parasitic feedthrough capacitance of $1pF$. At resonance the phase shifts from 180° to 0°. Due to the parasitic feedthrough, it shifts back shortly after. $f_0 \approx 49kHz$.

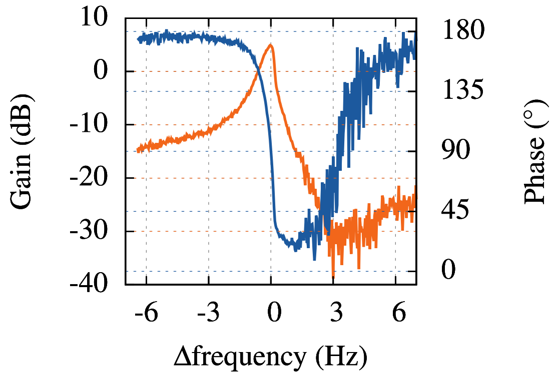

Figure 2.7: Measured transfer of a DETF structure without proper compensation of the parasitic feedthrough path. $f_0 \approx 49kHz$.

system behaves as expected at first. The gain sharply rises towards resonance and the phase has dropped 90° at resonance. Shortly after resonance, something strange happens. The gain drops more than expected and the phase does not drop towards 0°, but shoots up again to 180°. This extra phase shift is caused by the feedthrough capacitance [9, p. 253]. The larger this capacitance, the closer the two phase shifts are. Figure 2.7 shows a measured transfer where the feedthrough capacitance is not compensated. The additional phase shift is clearly visible and is very close to the actual resonance peak. The result is very noisy as the signal becomes very small at this point, the gain drops below $-30dB$ while the drive signal is only a few millivolts. In the end, to be able to make a stable oscillator system out of the DETF, the additional phase shift has to happen far enough away from the actual resonance peak. To push the additional phase shift a safe distance away from the actual resonance, the parasitic feedthrough capacitance has to be compensated. How this is accomplished is described in section 4.1.2.

2.4 Nonlinear behavior

In general it is good to drive the DETF structure at sufficient amplitude. This is beneficial for two reasons. Firstly, the signals in the readout electronics will be larger, improving noise performance there. Secondly, the resonance frequency of the DETF will remain more stable when sufficient energy is stored in the vibration [12]. The mechanical resonator itself is a source of noise in the system. The quality factor of the system can be made high, but it will always be finite. This means that there is always some dissipation happening in the system and all dissipation necessarily is a source of noise. Noise in the mechanical domain is not something people are used to. Luckily, the parallel with the electrical domain provides outcome. As shown in figure 2.5, the mechanical resonator structure can be represented by an electrical circuit. The finite quality factor of the resonator in this case is caused by the series resistor in the LC tank. Resistors dissipating energy in an electrical circuit are a well known source of noise and lots of methods exist to analyze and quantify this noise. The resistor represents the mechanical dissipation, which makes exactly the same methods available for analyzing noise in the mechanical domain. Mechanical noise can have many different origins and noise colors [8], but only the basic concept is needed here.

Taking into account the dissipative noise, the DETF is actually driven by 2 sources during operation: the drive signal and the noise source. For a constant quality factor, the noise power introduced by dissipation remains constant. It is therefore beneficial to increase the driving signal power to improve signal to noise ratio. Unfortunately, the vibration amplitude of a DETF cannot be made very large to cope with large signal powers. This is because nonlinearities in the system will cause hysteresis at large vibration amplitudes [12]. This destroys the resolution of the transducer structure, because hysteresis makes the sensor transfer multivalued.

The nonlinearities in the DETF originate from the spring constant. The standard second order model assumes that the restoring force is proportional to the rotor displacement and that the spring constant is in fact a constant. In general, this is not true and for large vibration amplitudes, this assumption no longer holds. In general, the spring constant can be approximated by a polynomial of arbitrary order. For small amplitudes, only including the zeroth-order term suffices. The larger the amplitudes, the more terms have to be considered. In this case terms up the second order are included, such that

$$c_{tot} = c_0 + c_1 x + c_2 x^2, \tag{2.16}$$

where c_0 is the linear spring constant and c_1 and c_2 are the first and second order corrections respectively. In this specific design, the nonlinearity in the spring constant is caused by two effects: spring hardening due to stretching of the DETF tines at large amplitudes and nonlinearity in the electrical spring constant from equation 2.2. The total capacitance from the DETF rotor to the readout electrodes can be approximated as in equation 2.7, but including higher order terms:

$$C_{tot} = \frac{4L_r t\varepsilon_0}{g}\left(\frac{1}{g-y} + \frac{1}{g+y}\right) \approx \frac{4L_r t\varepsilon_0}{g}\left(1 + \frac{y^2}{g^2} + \frac{y^4}{g^4}\right). \tag{2.17}$$

The nonlinear electrical spring constant then is given by

$$c_{el} = c_{el0} + c_{el1} y + c_{el2} y^2 \qquad \text{with:} \quad c_{el0} = -\frac{4V_b^2 L_r t\varepsilon_0}{g^3} \quad c_{el1} = 0 \quad c_{el2} = \frac{6c_{el0}}{g^2}. \tag{2.18}$$

The nonlinear spring constant resulting from spring hardening in the DETF tines can be approximated by assuming that the tine deforms with a triangular shape, and the nonlinear restoring force is caused by stretching of the tine. This results in a nonlinear spring constant of [12]

$$c_m = c_{m0} + c_{m1} y + c_{m2} y^2 \qquad \text{with:} \quad c_{m0} = \frac{192EI}{L_t^3} \quad c_{m1} = 0 \quad c_{m2} \approx \frac{0.767c_{m0}}{w_t^2}. \tag{2.19}$$

Combining these two contributions gives the coefficients c_n from equation 2.16:

$$c_0 = c_{m0} + c_{el0} = \frac{192EI}{L_t^3} - \frac{4V_b^2 L_r t\varepsilon_0}{g^3} \tag{2.20}$$

$$c_1 = c_{m1} + c_{el1} = 0 \tag{2.21}$$

$$c_2 = c_{m2} + c_{el2} = \frac{147.3EI}{L_t^3 w_t^2} - \frac{24V_b^2 L_r t\varepsilon_0}{g^5}. \tag{2.22}$$

This is an interesting result. The linear spring constant c_0 corresponds to the relevant part of the spring term in equation 2.12 and there is no first order nonlinear correction arising from the two considered effects. The most interesting part is the second order correction. Because of the negative sign of the nonlinearity introduced by the capacitive readout, it actually compensates part of the spring hardening. Moreover, since this nonlinear spring term depends on the bias voltage, it can be tuned such that the system is linear up to at least a third order correction. By exploiting this, the DETF driving amplitude can be increased, improving noise performance [11]. Experiments on this are treated in section 4.2.5.

The nonlinear differential equation that results from using a nonlinear spring constant is hard to solve and only implicit solutions exist. It is not instructive to include a full derivation here, so only

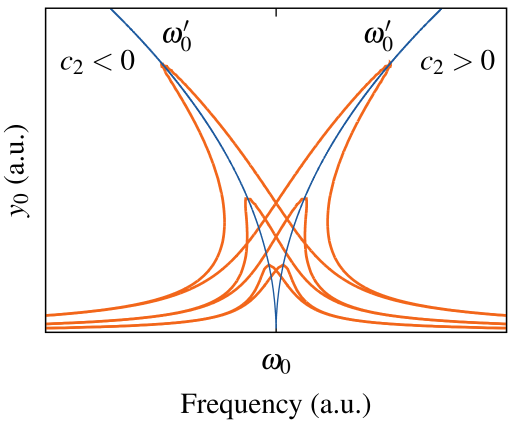

Figure 2.8: Nonlinear DETF transfer functions for different vibration amplitudes. The resonance frequency shifts down for $c_2 < 0$ and up for $c_2 > 0$.

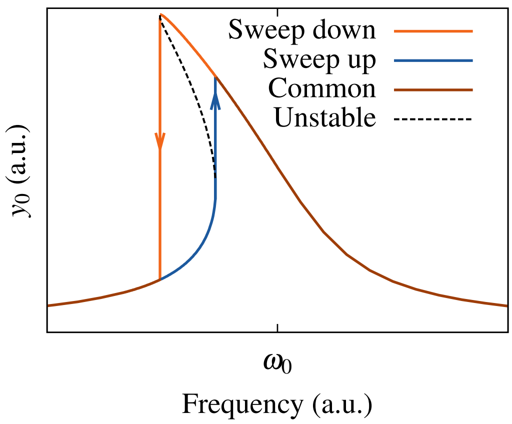

Figure 2.9: Hysteresis loop occurring for large vibration amplitudes. Measuring the transfer while sweeping the frequency up or down will give different results.

some important results will be included. For a more elaborate derivation of nonlinear effects, see [11, 12]. When the nonlinear effects become significant, the DETF resonance frequency becomes a function of the vibration amplitude y_0,

$$\omega_0' = \omega_0(1 + \frac{3c_2}{8c_0} y_0^2). \tag{2.23}$$

This effect is shown in figure 2.8. For a positive second order spring correction term, the nonlinear resonance frequency goes up with the vibration amplitude. For a negative c_2 it is the other way around. For very large vibration amplitudes, the transfer stops to be single valued for some driving frequencies around resonance. In a certain range of frequencies around the resonance peak, the transfer can take three values, of which the center branch is unstable. This results in measuring different transfers when sweeping the frequency up or down. Such a hysteresis loop is shown in figure 2.9. When the DETF is driven above the nonlinear limit and hysteresis occurs, the size of this hysteresis loop basically determines the resolution, because there is no way of knowing on which branch the system is operating at a specific moment. There is also a second disadvantage of nonlinearity that already manifests itself before hysteresis occurs. From equation 2.23 follows that any change in vibration amplitude causes a shift in the resonance frequency. When using the DETF as a sensing structure, such a frequency shift is indistinguishable from a shift caused by an axial load. Proper amplitude control therefore is important to improve the resolution of a DETF [6, p. 103].

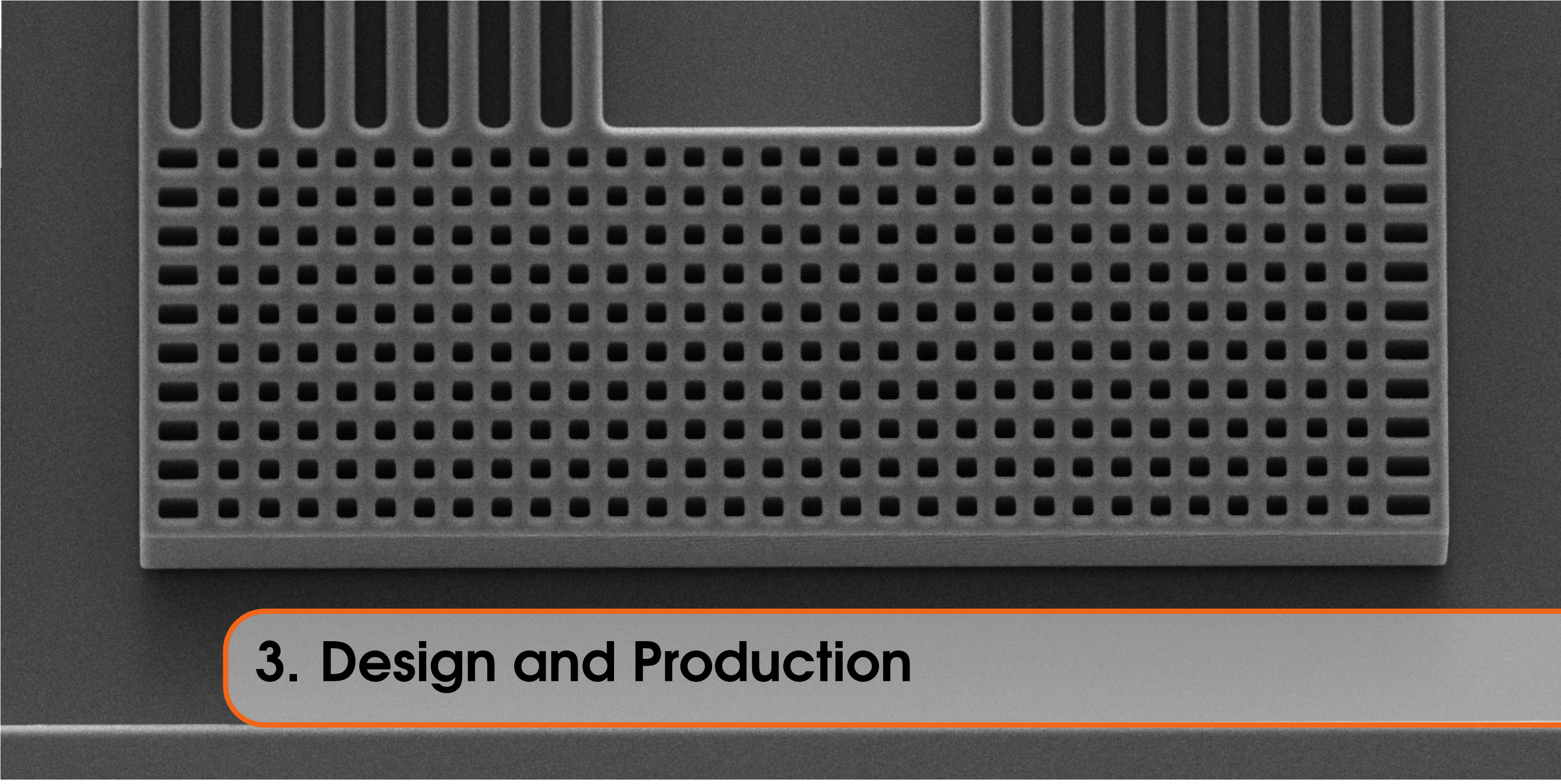

3. Design and Production

3.1 Production Process

The DETF prototypes are made using the so called SOI process. A SOI, or Silicon On Insulator, wafer is a wafer consisting of three layers. The thickest layer is the bottom layer consisting of silicon. This layer is called the handle layer. The top layer also consists of silicon, but is much thinner than the handle layer. This top silicon layer is the most important, as devices will be defined here. This layer is therefore called the device layer. The device layer in this case is $25\mu m$ thick and all defined structures will therefore share the same thickness. In between the silicon layers, there is a $2\mu m$ thick buried oxide layer, or BOX-layer for short.

A schematic representation of a processed wafer is shown in figure 3.1. The top and bottom silicon layers can be patterned using photolithography and an anisotropic dry etching step. This way, silicon can be removed at defined places while silicon structures with straight walls remain. As a final step, parts of the device layer are released from the handle layer by selectively removing parts of the BOX-layer with HF vapor. The vapor enters through the holes in the silicon and removes the exposed oxide. Where the exposed oxide is removed, the HF vapor can also etch the oxide under the silicon structures, fully releasing any small silicon parts. When the etching process is stopped in time, large silicon parts in the device layer will remain attached to the handle layer through a patch of oxide, as illustrated in figure 3.1. A complete description of the process is given in appendix B.

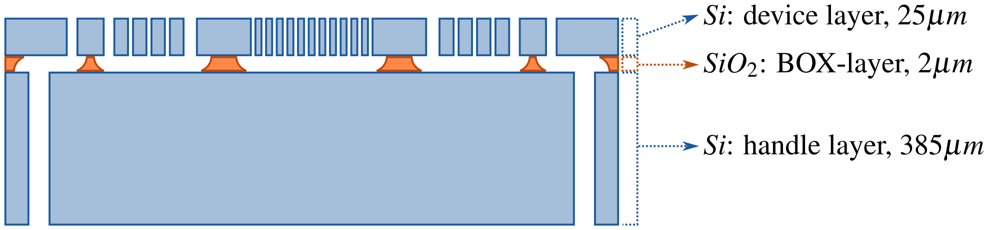

Figure 3.1: Schematic representation of a processed SOI-wafer.

3.2 Device Design

To gain insight in the behavior of the DETF structure, a MEMS device was designed to be produced in the given SOI-process. The most important aspect of this design is its ability to apply axial loads to the DETF structure in a controllable way. In figure 3.2, an overview picture of the MEMS device is shown. From bottom to top it consists of:

1. Double ended tuning fork
2. Force guiding roller
3. Force amplification levers
4. Compression springs
5. Ratchet
6. Thermal actuator

In summary, the thermal actuator (6) pushes a ratchet (5) that transforms the small actuator strokes in a large displacement. The springs (4) are compressed this way and the resulting force is amplified by a set of levers (3). The roller structure (2) transfers this force as an axial load onto the DETF (1). The separate building blocks will be discussed further in this section.

In addition to the main structure, different diagnostic structures are incorporated on the device to further test the effects of the capacitive readout plates on the operation of the DETF. These are just DETF structures with different dimensions with no option to apply axial loads. As these structures are identical to the DETF used in the main structure, only the building blocks of the main structure will be discussed in this section.

3.2.1 DETF structures

The DETF tines are simple silicon beams that are $10\mu m$ wide. This is the maximum width that can still be released from the handle layer in this production process. Multiple DETF structures are realized on one silicon die and tines of different lengths are incorporated in the design. DETF structures with tines of three different lengths ($700\mu m$, $800\mu m$ and $1000\mu m$) are included to test the dependence of the DETF resonance frequency on the tine length.

An important feature of the DETF structure is the point where the tines are anchored. This anchor point is shown in figure 3.3. The two DETF tines are connected to a perforated silicon block and this block is connected to the fixed part of the device layer on the other end. The perforation ensures that this anchor block is not connected to the handle layer. If the anchor block would have been fixed to the handle layer, energy could have radiated through the anchors, hereby reducing the quality factor. Constructing the DETF like this and operating the tines in anti-phase, the resulting force and moment on the anchor block will be zero at all times. This way, anchor motion is minimized and the quality factor is only limited by internal material losses when operated in vacuum environments [16].

Because of the expected high quality factor of the system, the amplitude of vibration is hard to predict. The capacitive gap is quite small and when for some reason the vibration amplitude becomes too large, the rotor could touch the stator electrodes. When this happens, a short circuit is introduced, possibly permanently damaging the structure. To avoid this, mechanical stops are positioned around the T-junction of the readout plate. The gap here is $500nm$ narrower than the capacitive gap, so that with moderate bias voltages, the rotor can never touch the stator electrodes. These mechanical stops are shown in figure 3.4.

The DETF structures are designed to operate around $50kHz$ after the structures in [3]. The dimensions corresponding to this design are shown in table 3.1. In the third column the dimensions as fabricated are given as well. These values are measured with a SEM on fabricated devices and will be used for the theoretical predictions when interpreting the measurement results.

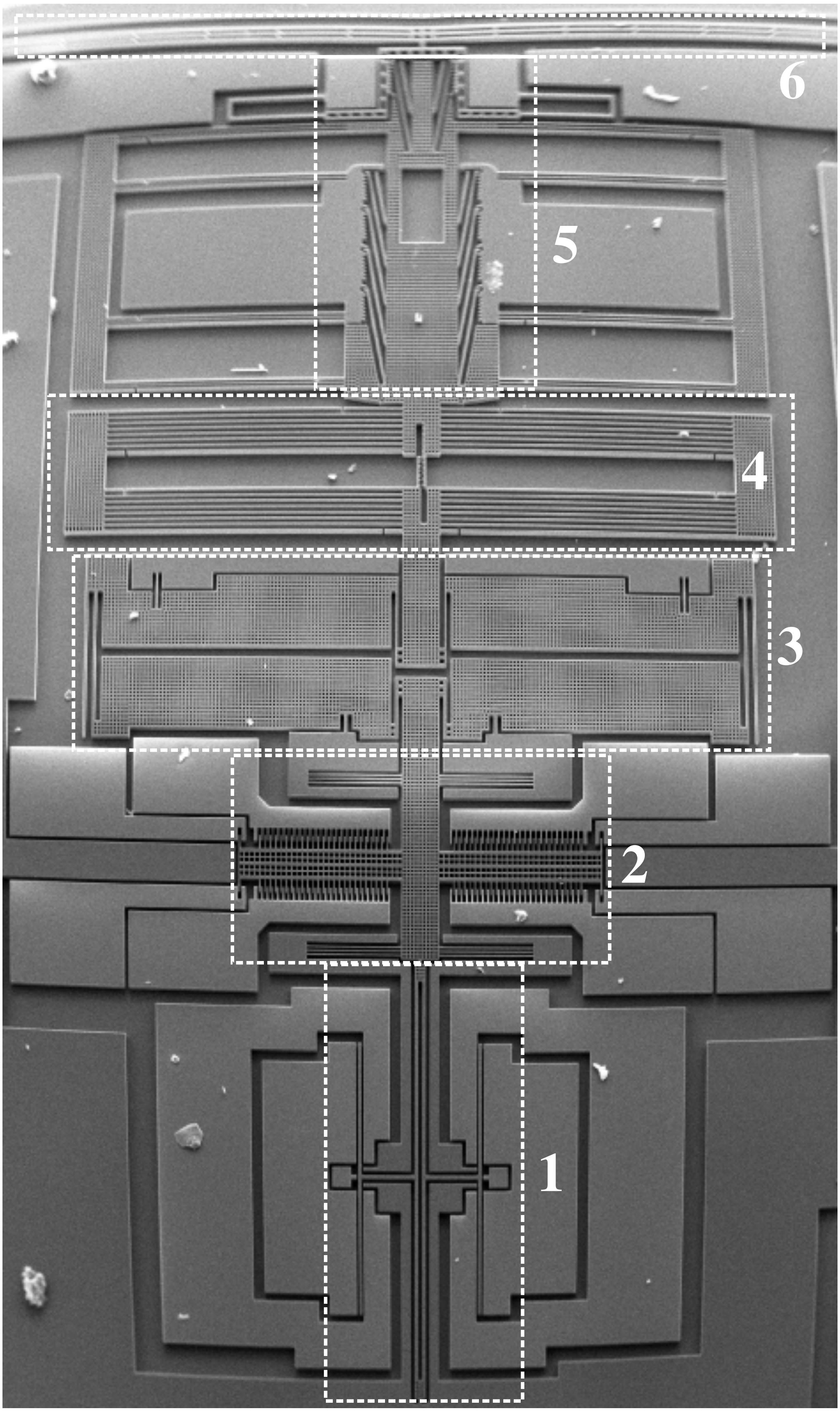

Figure 3.2: Overview image of the MEMS structure to apply axial loads to the DETF structure. Indicated in the picture: 1. DETF, 2. Force guiding roller, 3. Force amplification levers, 4. Compression springs, 5. Ratchet, 6. Thermal actuator.

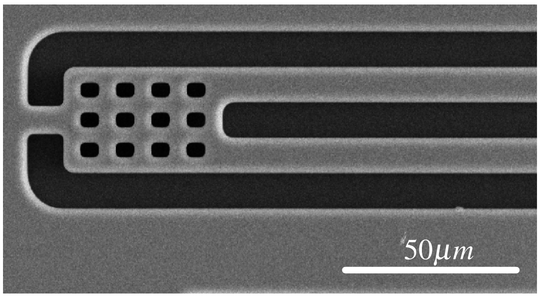

Figure 3.3: The DETF anchor. The two DETF tines are shown on the right. They are anchored to a perforated block that is released from the substrate. The block is then connected to the fixed part of the device layer.

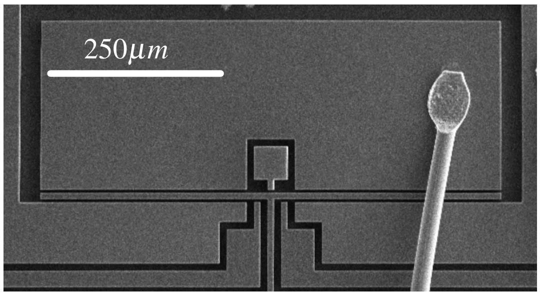

Figure 3.4: The T-shaped capacitive readout structure. Close to the T-junction, 3 mechanical stops are positioned such that the readout beam is unlikely to make a short-circuit.

Dimension	Designed value	As fabricated
L_t	$700/800/1000\mu m$	$700/800/1000\mu m$
L_c	$140\mu m$	$140\mu m$
L_p	$680\mu m$	$680\mu m$
L_r	$305\mu m$	$305\mu m$
t	$25\mu m$	$25\mu m$
w_t, w_c, w_p	$10\mu m$	$9.7\mu m$
g	$4\mu m$	$4.3\mu m$

Table 3.1: DETF dimensions (see figures 2.1 and 2.2).

3.2.2 Loading roller

To test the response of the DETF to axial loads, a roller has to be added that can transfer forces to the tuning fork and ensures that these forces are only transferred in its axial direction. A structure that does this is shown in figure 3.5. The roller structure is indicated within the dashed box. It consists of a central perforated block on which different forces can be exerted, and four sets of guiding springs. At the bottom, the block is connected to one end of a DETF. The guiding springs can be simply made of clamped-clamped beams, because the expected displacement is really small.

The guiding beams are relatively stiff. They are $4\mu m$ wide and $250\mu m$ long each, which gives a total stiffness of about $210N/m$ in the direction of the DETF. This is not an issue, because the axial stiffness of the DETF structure is much higher, about $85kN/m$. The guiding springs will therefore only lower the applied force with about 0.2%, which is negligible. The advantage of using multiple short beams placed some distance apart is that the stiffness of the other two in plane degrees of freedom is very high. Stiffness in the direction perpendicular to the DETF is about $815kN/m$ and in-plane rotation is blocked by this same highly stiff direction. For calculations on beam stiffness, see appendix A.1.

The comb structures attached to the side of the roller block are designed to exert small forces on the DETF. The large comb arrays consist of 25 teeth in each of the four quadrants of the roller. A force can be exerted in both tensile (up) and compressive (down) direction. Each direction uses 50 teeth that are separated from the stator teeth by a gap of $3.5\mu m$, which is the minimum gap size allowed in the production process. The force exerted by a combdrive actuator is given by [5, p. 194]

$$F_{comb} = \frac{Nt\varepsilon_0}{g_{comb}}V^2, \tag{3.1}$$

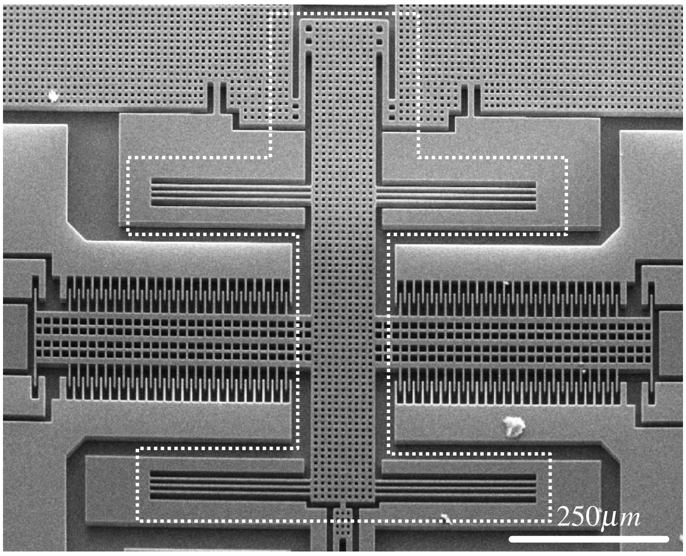

Figure 3.5: SEM image of the roller structure that is used to transfer axial forces to the DETF. The roller structure is shown within the dashed box. Combdrive actuators are attached to it to apply very small forces and levers are attached to the top end to transfer large forces.

where N is the number of comb fingers, ε_0 is the vacuum permittivity and g_{comb} is the comb capacitive gap. When the comb arrays are actuated between 0 and $50V$, this results in a maximum applicable force of $8\mu N$ to either side. Fringing fields will increase the applied forces somewhat, but for an order of magnitude estimation, this approximation will do. Using the geometry of the DETF and the expression for the resonance frequency in equation 2.12, these axial forces will lead to at least a $14Hz$ change in resonance frequency, which should be easily detectable.

Next to the comb actuator array, there is also an actuator structure that has only one tooth. This one is included to be able to exert very accurate forces when the stability of the DETF turns out to be very good. The resolution of this actuator is 25 times better than the array actuator, but the maximum force it can exert is of course 25 times lower.

3.2.3 Lever structure

To investigate the response of the DETF structure over a large force range, also large forces need to be applied to the roller structure. The most interesting effects happen around the point where the DETF will start to buckle. The buckling force of a DETF structure is relatively high. Taking the $1000\mu m$ long DETF will give the lowest buckling load of [15, p. 106]

$$F_{buck} = -2 \cdot \frac{4\pi^2 EI}{L^2} \approx -26mN. \tag{3.2}$$

In the context of MEMS devices, $26mN$ is a very large force that is hard to generate directly. Therefore, some form of force amplification is needed.

To this end, a set of levers has been designed that transfer a force with an amplification factor of approximately 20. The lever structure is shown in figure 3.6. A force can be exerted on the block shown in the top center of the figure. Through two slender silicon beams, this force is transferred to two large blocks that can rotate around the pivots shown in the dashed boxes. The other end of the first lever block is connected through another (slightly thicker) slender beam to the second lever. The ratio $L_{11} : L_{12}$ is $4 : 1$ for the first lever, such that the force that is transferred to the second lever is already four times larger than the input force. The second lever block repeats this trick, but this

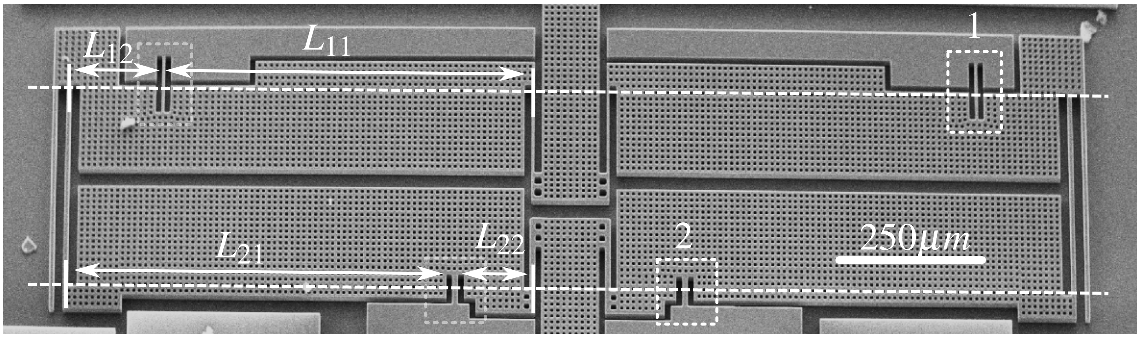

Figure 3.6: SEM picture of the force amplification levers. A downwards force can be exerted on the top block in the center of the structure. Two sets of levers amplify this force with a factor of 20 and transfer it to the roller that can be seen at the bottom center. Lever pivots are indicated in the dashed boxes.

time $L_{21} : L_{22}$ is 5 : 1 to arrive at a total designed force multiplication of 20 times. The output of the second lever is connected to the roller block, so that the output force is directly transferred as an axial load on the DETF.

A few things are worth noticing about the lever design. Firstly, while progressing from input to output, the connecting beams and pivots become wider and stiffer. This is to be able to handle the stresses that keep increasing towards the output as well. All the slender connecting beams and pivot beams are loaded in tension because that way they can handle significantly higher loads. Secondly, the force input and output of a lever block are on one line with the center of the pivot beam, as is indicated by the dashed lines in figure 3.6. This is done because the virtual center of rotation of a flexure with the load case used here, can be approximated to be in the center of the pivot beam for small deflections [15, p. 90]. Keeping the force input and output on one line with the center of rotation, will ensure that the force transmission ratio will remain unchanged, even under small rotations.

A disadvantage of using such short beam flexures as a pivot structure, is that they possess a rotational stiffness themselves. It is important that this stiffness is not too large as compared to the stiffness of the DETF structure, otherwise only a fraction of the input force is amplified and transferred to the DETF structure. The rotational stiffness of a beam flexure is given by [15, p. 98]

$$c_{rot} = \frac{4EI}{\ell}, \tag{3.3}$$

where ℓ is the length of the beam flexure. This rotational stiffness can be transferred to a linear stiffness at the force input of a lever block by dividing by the lever length squared,

$$c_{lever} = \frac{4EI}{L_{x1}^2 \ell}, \tag{3.4}$$

where L_{x1} is the input length of the lever block as shown in figure 3.6. Translating the pivot stifnesses and the DETF stiffness to the input of the lever structure gives [15, p. 2]:

$$c_{pivot1} = \frac{4EI}{L_{11}^2 \ell} \approx 4.32N/m \tag{3.5}$$

$$c_{pivot2} = \frac{4EI}{L_{21}^2 \ell} \cdot \frac{1}{4^2} \approx 3.96N/m \tag{3.6}$$

$$c_{DETF} = 2\frac{w_t t E}{L_t} \cdot \frac{1}{20^2} \approx 212.5N/m \tag{3.7}$$

This means that the total stiffness seen at the input is approximately $229N/m$ and that approximately 93% of this is caused by the DETF stiffness. This also means that only 93% of the force that is

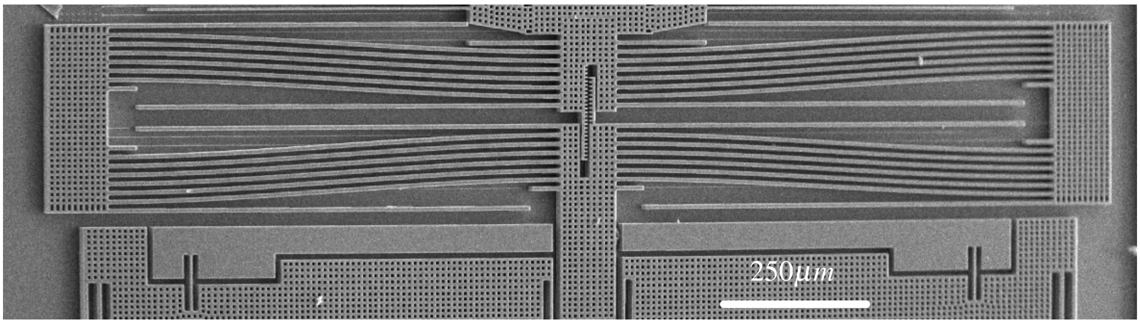

Figure 3.7: SEM picture of the spring structure that generates the force on the input of the lever structure that can be seen at the bottom. The structure is shown in a compressed state. The displacement of the top block can be accurately measured from the lever structure in the center. A closeup view is shown in figure 3.8.

input is amplified and transferred to the DETF. Finite element simulation was used to confirm this analysis. One half of the lever structure was used as a simulation geometry. The pivots were fixed at the ends and the lever output was connected to a finite stiffness representing the DETF stiffness. A force that is applied to the input is transferred to the output amplified with a factor of 18.8, which is 94% of the designed value of 20. This corresponds very well to the previous analysis. The effective multiplication factor of the levers that will be used in handling the results is 18.6.

3.2.4 Force Generator

The structure that generates the input force on the levers consists of several parts. A thermal actuator generates a relatively large force with a limited stroke. A ratchet structure transforms this small stroke in a large displacement and finally this displacement is transferred to a force by a set of springs.

The springs are shown in a compressed state in figure 3.7. The total structure is implemented using a folded flexure to allow for large displacements. This flexure is attached to a block that leads to the levers at the bottom. At the top it is connected to the end of the moveable ratchet block. The total folded flexure consists of 24 spring beams of $800\mu m$ long and $7.4\mu m$ wide. These 24 beams are divided in 4 groups of 6 giving a total stiffness of $20.2N/m$. This is about 10 times lower than the input stiffness of the levers which means that the lever input will displace 10 times less than the compression of the spring set. This is ample to build up sufficient force. A closer look at figure 3.7 reveals that each group of spring beams is surrounded by beams that are not connected all the way through. These dummy beams serve no mechanical purpose, but are there to provide a similar environment for all spring beams during the etching process. This ensures that all walls are etched equally fast and equally straight. Similar structures can be encountered at many places where proper etching profiles are important.

Recalling from section 3.2.3 that the DETF buckling load is $26mN$ and that the levers amplify force with a factor 18.6, the force that needs to be generated by the springs is at least $1.4mN$. With a spring constant of $20.2N/m$ this translates to a displacement of about $75\mu m$. $75\mu m$ is a large displacement for such relatively stiff springs. The maximum stress occurring at the ends of the spring beams at this displacement is approximately $220MPa$ [15, p. 99]. The yield strength of silicon varies a lot from source to source. As a rule of thumb, it is unwise to load silicon structures above $300MPa$. As the maximum stress is still only two thirds of that value, the springs will most likely hold the maximum load to be applied.

In the end, the force that is exerted on the DETF is determined by measuring the compression of the spring structure. To accurately determine this compression, a special calipers structure is included. A close up of this structure is shown in figure 3.8. Using this structure, the compression can be measured to at least 1 part in 10 of the period on the calipers. This period is determined by

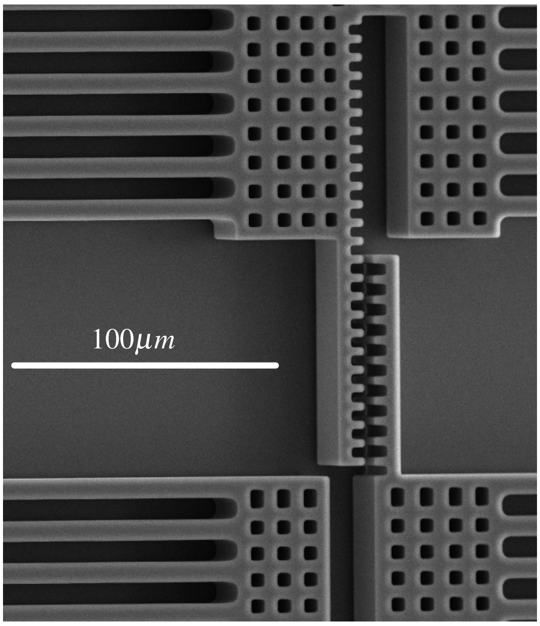

Figure 3.8: SEM picture of the calipers structure used to accurately measure the spring compression. From this compression the DETF load can be calculated.

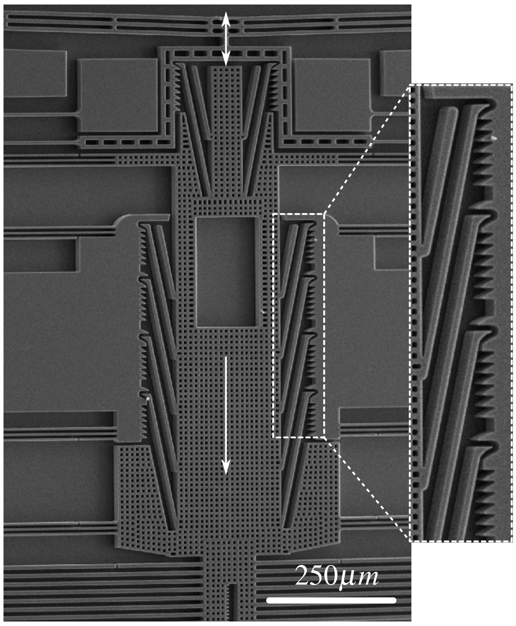

Figure 3.9: SEM picture of the ratchet structure. At the top it is driven by small strokes of a thermal actuator, the ratchet in the inset ensures motion in one direction only.

the minimum feature size of the etching process and is 7μm in this case. Compression can therefore be determined with at most 700nm deviation.

The large displacement is generated by a thermal actuator driving a ratchet structure. This structure is shown in figure 3.9. The center part of the thermal actuator is shown in the top of the picture. By sending a current through the actuator beam, it heats up and expands. Because the two halves of the actuator beam meet at an angle in the center, this center point moves down when the beam expands. During expansion, the center part of the actuator pushes a ratchet structure. The thermal actuator has limited stroke, but the ratchet can convert this in a large displacement by only allowing motion in one direction. When the thermal actuator cools down, it moves back to its original position. The springs and teeth shown in the inset of figure 3.9 prevent the ratchet block from moving back, and each next thermal actuator stroke will push the block one step further. The teeth are spaced 10.5μm apart, but the 4 sets of teeth shown are positioned at offset positions. This way the step size of the ratchet block reduces to about 2.6μm.

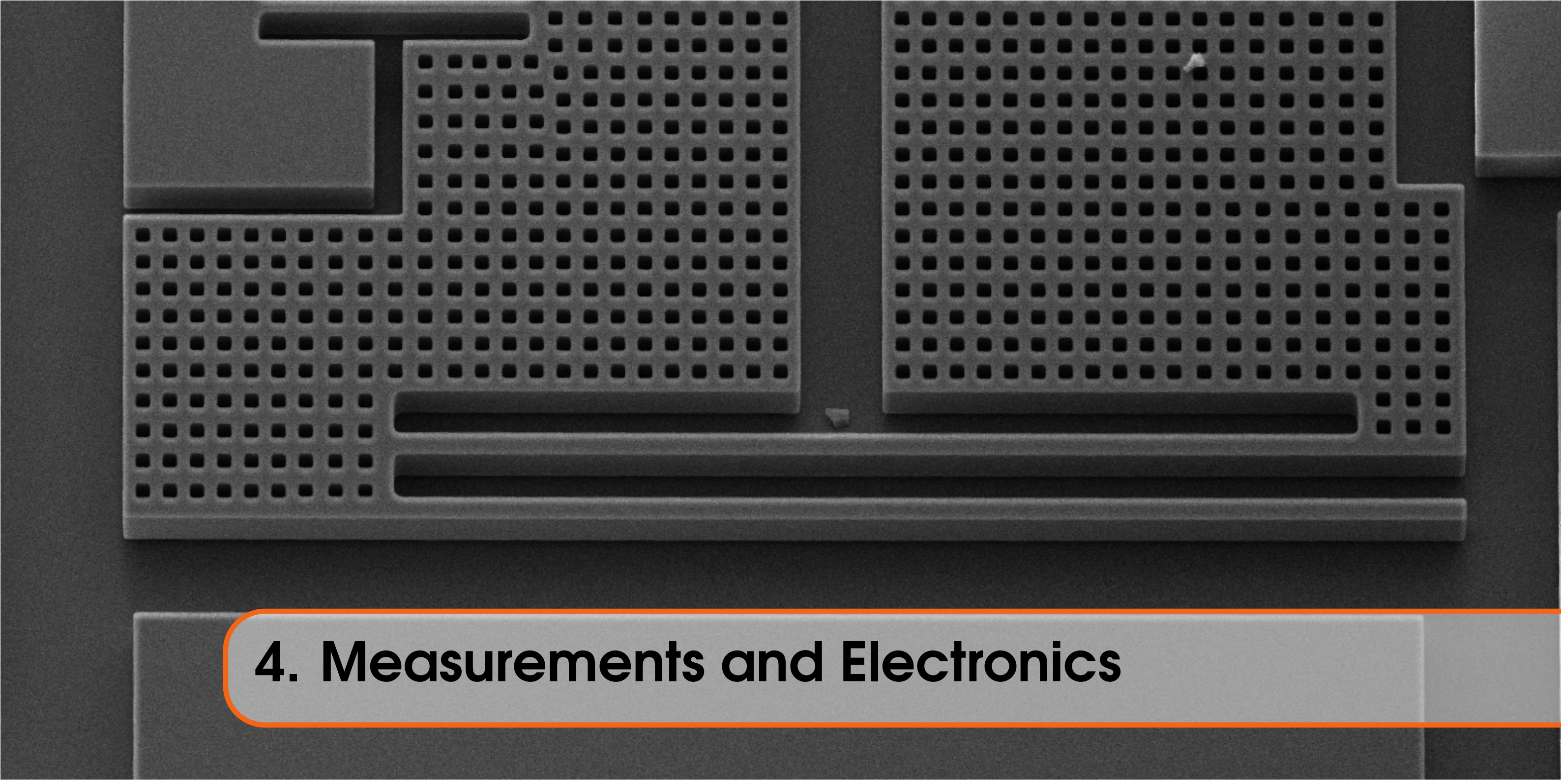

4. Measurements and Electronics

In this chapter an overview will be given of the DETF properties that are measured. Results will be discussed and compared to the theoretically expected behavior from chapter 2. Firstly, however, some details of the measurement setup need to be discussed.

4.1 Measurement setup

The measurement setup basically consists of three main parts: a charge amplifier, a compensation amplifier and a gain-phase analyzer. A schematic overview of the system is given in figure 4.1. The DETF readout electrodes are biased at V_b through two large resistors R_b. This charges the DETF readout capacitances as is needed to get a signal. The gain-phase analyzer drives the DETF with a small actuation voltage v_{drive} through a large coupling capacitor C_c. This driving signal is directly brought to the output through a compensation amplifier to compensate most of the parasitic feedthrough capacitance that exists between the input and the output of the DETF. The charge amplifier at the output transforms the output current to a voltage, v_{sense} that can be measured by the gain-phase analyzer. In this section some important aspects of both parts of the system will be discussed.

4.1.1 Charge amplifier

The charge amplifier is implemented using an AD8066 high speed opamp. It's schematic is shown in figure 4.2. Any input current will flow through the feedback network consisting of C_f and R_f. In the frequency band of interest, $30kHz - 100kHz$, the feedback network impedance is dominated by C_f. The current will therefore flow through C_f, charging the capacitor. The amplifier output voltage will be proportional to the charge on the capacitor, hence the name charge amplifier. The large feedback resistor R_f is included to provide a DC feedback path.

The amplifier was calibrated by measuring the gain with different capacitance values connected to the input of the amplifier. Because the gain of the amplifier is given by C_{in}/C_f, the effective value of C_f can be accurately determined this way. The calibration results are shown in figure 4.3 and the resulting value for C_f is $5.2 \pm 0.1 pF$. This value is important for accurately determining the current coming out of the DETF. The gain in the frequency band $30kHz - 100kHz$ remains

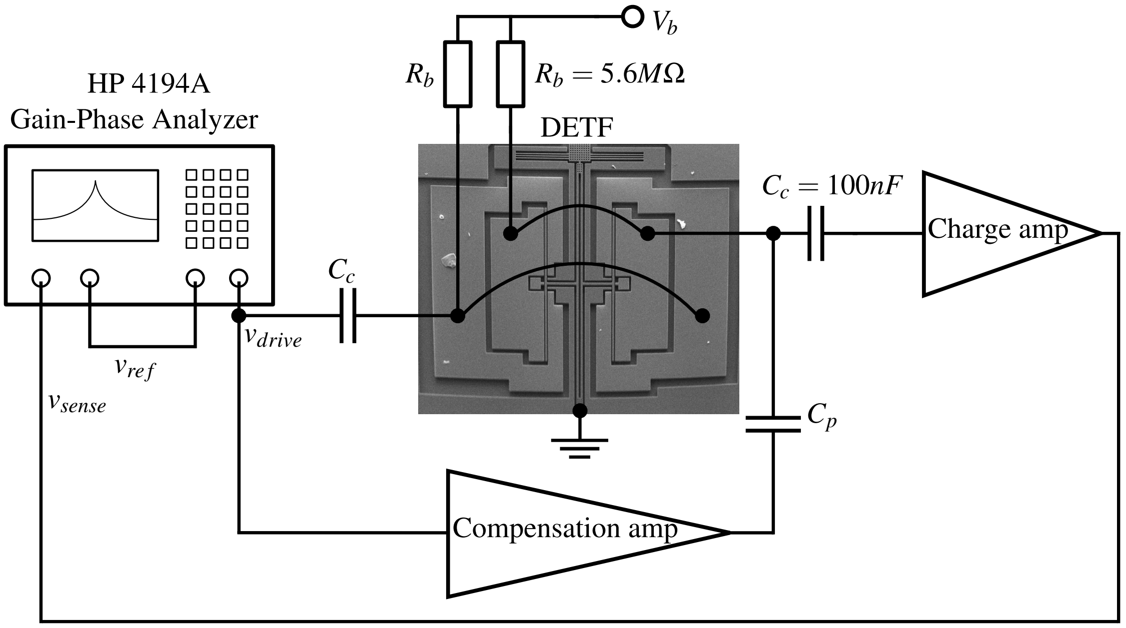

Figure 4.1: A schematic overview of the measurement setup. The DETF readout electrodes are biased through large resistors R_b. The gain-phase analyzer drives the DETF through a large coupling capacitor C_c. A charge amplifier transfers the output current to a voltage that can be measured by the gain-phase analyzer.

constant to within $0.1dB$ and the introduced phase shift varies from $180-8°$ to $180+3°$. This phase shift, however, happens very gradually and will therefore have no significant influence on measuring the phase shift around resonance.

4.1.2 Compensation amplifier

As described in section 2.3, there will always be some parasitic feedthrough capacitance between the input and output of the DETF. This capacitance introduces an extra unwanted phase shift close to the resonance frequency of the system [9, p. 253]. To decrease this effect, the parasitic capacitance can be largely removed by introducing another feedthrough capacitance with opposite sign. Both the feedthrough paths simply add, and the total feedthrough capacitance can be made much smaller by setting the negative capacitance to the right value. The compensation amplifier shown in figure 4.4 implements this negative capacitance as an inverting amplifier with tunable gain driving a small

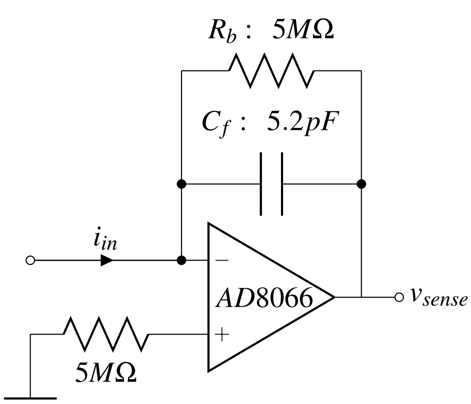

Figure 4.2: Electrical schematic of the charge amplifier.

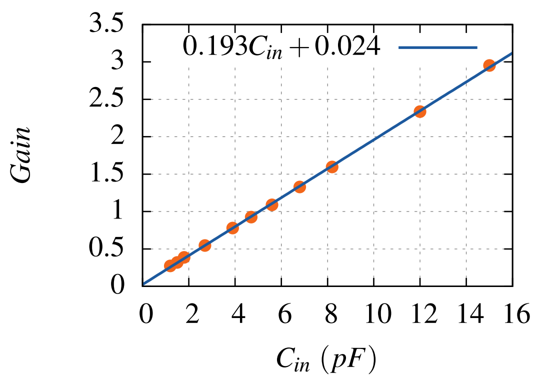

Figure 4.3: Charge amplifier calibration curve.

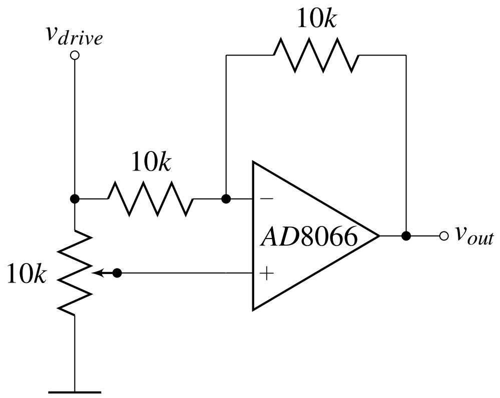

Figure 4.4: Electrical schematic of the compensation amplifier. The gain can be controlled between -1 and +1 through the potentiometer.

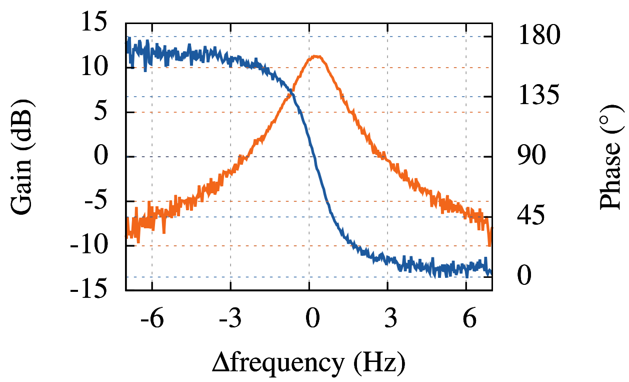

Figure 4.5: A typical measured DETF transfer around $f_0 = 74.312Hz$. The gain (orange) and phase (blue) are in dB and degrees respectively, measured relative to v_{drive}.

series capacitance, C_p. Due to the small phase shift the amplifier introduces, the feedthrough can never be totally eliminated, but it can be reduced significantly.

4.1.3 Gain-phase analyzer

The gain-phase analyzer has two drive ports that output the same signal. One of these ports is used to drive the DETF structure, the other one is looped back to the reference input, as is shown in figure 4.1. The drive levels can be varied, but are not very accurately defined. This does not matter for accurately determining the gain and phase, but is important for estimating the DETF vibration amplitudes. The drive levels are determined using an oscilloscope for better accuracy.

4.2 Measurement results

4.2.1 Quality factor

Having a high quality factor is good for the stability of the system and makes it easier to accurately determine the resonance frequency. To achieve such a high quality factor, the entire system is operated in a vacuum environment. The DETF quality factor was measured from transfer curves taken by the gain-phase analyzer, such as the one shown in figure 4.5. Using electronics to measure a mechanical quality factor influences the measurements by introducing extra electrical losses into the system. To get an accurate result for the purely mechanical quality factor, it is important to know how large these losses are.

Equation 2.1 states that the current flowing in and out of the readout capacitors is proportional to both the speed of the capacitor plate, $\dot{y}$, and the bias voltage on the electrode. The power lost in any resistive part of the electronic readout circuit impedance is proportional to the current squared. This leads to an electrical damping force on the DETF of [19]

$$F_{el} = -\eta^2 R_{circuit} \cdot \dot{y} = -\gamma_{el} \cdot \dot{y}, \tag{4.1}$$

where $R_{circuit}$ is the resistive part in the readout impedance. The resulting damping coefficient, γ_{el}, defines an electrical quality factor that depends on the bias voltage. This quality factor adds to the already present mechanical quality factor to get the total measured quality factor of the system [19]:

$$\frac{1}{Q_{tot}} = \frac{1}{Q_{mech}} + \frac{1}{Q_{el}}, \tag{4.2}$$

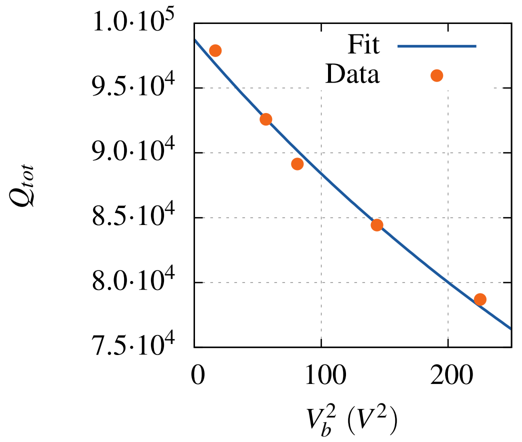

Figure 4.6: Measured quality factors at different bias voltages V_b. The blue line represents a fit to extract the mechanical quality factor.

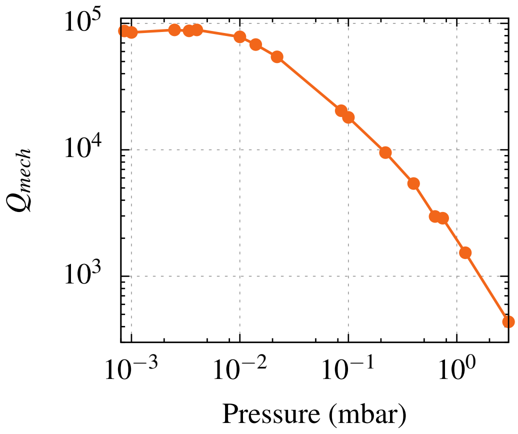

Figure 4.7: Extracted mechanical quality factors for different vacuum chamber pressures. For low pressures the curve saturates to $98.7 \cdot 10^3$.

where $Q_{el} = m_{eff}\omega_0/\gamma_{el}$. The value for $R_{circuit}$ is unknown, but equation 4.1 shows that the electrical quality factor is proportional to $1/\eta^2$ and therefore to $1/V_b^2$. Recalling the MEMS electrical equivalent in figure 2.5 can conceptually confirm this proportionality. The $1:\eta$ transformer that couples the electrical to the mechanical domain transforms voltages as $1:\eta$ and currents as $1:1/\eta$. This means that the impedance seen looking into the transformer from the mechanical domain scales as η^2. The damper in the mechanical domain is modeled as a resistor. Any restive part of the readout circuitry will add to this damping resistance as $\eta^2 R_{circuit}$, arriving at the same conclusion.

While the exact value for $R_{circuit}$ remains unknown, the $1/V_b^2$ proportionality can be fitted to measured data to extract the mechanical quality factor. In figure 4.6, measurement results are shown for the DETF quality factor for different bias voltages. The figure shows clearly that the measured quality factor drops with higher bias voltages. This results correspond well to the proposed electrical damping model, which is fitted as the blue line in the figure. The mechanical quality factor can be extracted from the intersection with the y-axis and is $98.7 \cdot 10^3 \pm 2.7 \cdot 10^3$ where the error bounds indicate the 95% confidence interval.

The fit in figure 4.6 also defines the electrical quality factor for a specified bias voltage. This result can be used to directly correct measurements conducted with a specific bias voltage to obtain the mechanical quality factor. In figure 4.7 results for the mechanical quality factor are shown as a function of pressure. As can be seen in the figure, the mechanical quality factor is limited by air damping for pressures higher than 10^{-2}mbar. For lower pressures, the quality factor is limited by losses in the DETF structure itself. This internal loss is dominated by thermoelastic damping, which can be approximated using Zener's model. This provides an upper limit for the reachable quality factor for this geometry of approximately $120 \cdot 10^3$ [7]. The extracted quality factor reaches this limit to within 20%, which means that other loss mechanisms are not dominant and the DETF anchors perform well dynamically. To ensure that the quality factor is as high as possible at all times, following measurements will be conducted below 10^{-2}mbar.

4.2.2 Bias voltage

The bias voltage does not only influence the DETF quality factor, but it lowers its resonance frequency as well. The resonance frequency without the presence of a bias voltage cannot be measured, because without the bias, there is no signal to read out. However, a trick similar as with the quality factor can be used to eliminate the effect of the bias voltage on the resonance

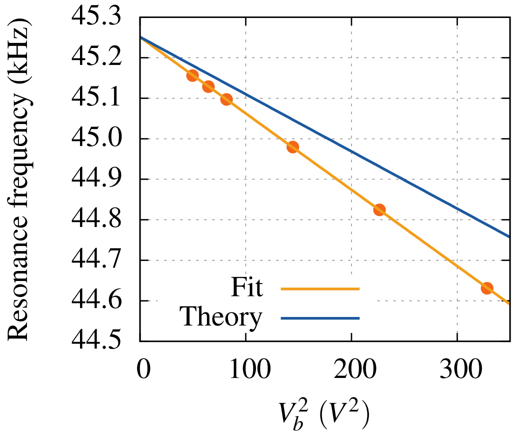

Figure 4.8: Dependence of the DETF resonance frequency on the readout bias voltage, along with its theoretical prediction and a linear fit.

frequency in the results. Because the influence of the bias voltage will in general be small, the DETF resonance frequency can be approximated by a first order Taylor series in V_b. Expanding the resonance frequency given in equation 2.12 gives

$$\omega_0 \approx \omega_0|_{V_b=0} + V_b \cdot \left.\frac{\partial \omega_0}{\partial V_b}\right|_{V_b=0} = \omega_{0,mech} - \alpha V_b^2 \tag{4.3}$$

$$\text{with} \quad \alpha = \frac{2L_r t \varepsilon_0}{(\frac{13}{35}\rho L_t w_t t + m_c) \cdot g^3 \omega_{0,mech}}$$

in which $\omega_{0,mech}$ denotes the mechanical DETF resonance frequency without the effect of the bias voltage. It can be determined by measuring the DETF resonance frequency at multiple different bias voltages and fitting equation 4.3. Such a measurement is shown in figure 4.8. The linear fit follows the measured data very accurately. The mechanical resonance frequency can be accurately determined from the intersection with the y-axis. The theoretical curve resulting from equation 4.3 is plotted in the same figure. The theoretical slope α is somewhat lower than the measured one. This was to be expected, because it has been derived using the naive parallel plate approximation for the readout capacitance. The capacitor plate dimensions are quite comparable to the gap between the plates, so in reality the capacitance will be significantly higher due to fringing fields. This also results in a higher measured value for α.

4.2.3 Axial loads

The transduction principle of the DETF is based on the change of the resonance frequency with axial loads. To check the validity of equation 2.12, the mechanical resonance frequency was extracted as before for different compressive axial loads. This means that the effect of the bias voltage on the readout electrodes is eliminated from the results, but also that each measurement had to be repeated at many different bias voltages. The purely mechanical resonance frequency is obtained by the intersection with the y-axis, just as in figure 4.8. Unfortunately, this made the process very time consuming. Adding to this is the fact that the thermal actuator was not strong enough to overcome the static friction introduced in the ratchet structure. This meant that for changing the axial load on the DETF, the entire system had to be disassembled, the ratchet structure had to be manipulated manually with micrometer precision and after reinstalling the setup, the high-vacuum system had

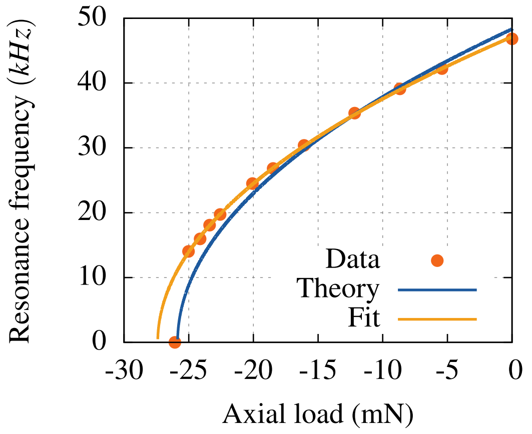

Figure 4.9: Resonance frequency of a DETF with 1000μm long tines as a function of axial load. Axial load was calculated from measured spring compressions.

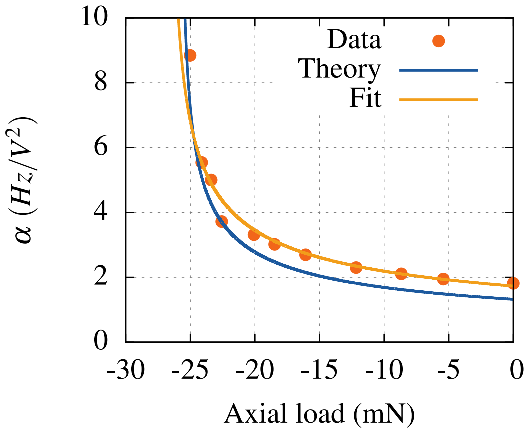

Figure 4.10: The sensitivity of the resonance frequency of a DETF with 1000μm long tines to the bias voltage (equation 4.3) as a function of the applied axial load.

to settle again. Especially the manual manipulation of the ratchet structure cost a lot of time. Not in the least because multiple devices got broken during this process.

The results that were eventually extracted are shown in figure 4.9. Comparing the data with the theoretical expectation (in blue), it can be seen that the theory slightly overestimates the resonance frequency for no axial load. This effect is seen in all the measured resonators and is probably caused by a finite stiffness of the anchor points of the DETF tines. Furthermore, the scaling of the x-axis is a bit off when comparing the data points to the theory. Determining the exact force that was applied to the DETF is hard. The displacement of the compression springs was accurately measured to provide a scale for the applied force. Converting these displacements to a force was done using the theoretical lever amplification from section 3.2.3 and the calculated spring constant from section 3.2.4. These values will very likely be off by a few percent. Unfortunately, using this setup, there is no way to directly measure the lever amplification and the relevant spring constant, so going by the theoretical predicted values is the only in this case. Fortunately, the predicted shape corresponds quite well to the measured data. This is confirmed further by fitting the theory to the data with two additional scaling parameters, one for each axis. As can be seen in figure 4.9, the measured data follows such a fit very closely, confirming that the functional form of the model is correct, but that the force scaling is off.

Figure 4.9 also shows that the DETF buckles at a somewhat smaller load than the fit predicts. This can be attributed to multiple effects. Firstly, the DETF model in equation 2.12 and the classical buckling formula in equation 3.2 predict slightly different buckling points. Going by the classical buckling formula, the DETF should already buckle at a load about 1.5% lower than that predicted by the DETF model. Secondly, the buckling formula is the result of a static analysis while the DETF is constantly actuated away from its stable equilibrium point. The buckling load becomes a function of the DETF vibration amplitude, which is not included here. It is not strange that the structure buckles somewhat sooner than expected.

In figure 4.10 the sensitivity of the DETF resonance frequency to the bias voltage as predicted by equation 4.3 is shown. As expected from section 4.2.2, the theory consequently underestimates the DETF sensitivity to the bias voltage. Fitting the results with the same technique as with the resonance frequency, a curve is found that corresponds quite well to the measured data. The resulting scale factor for the force axis is approximately the same as for figure 4.9, they differ about 2%.

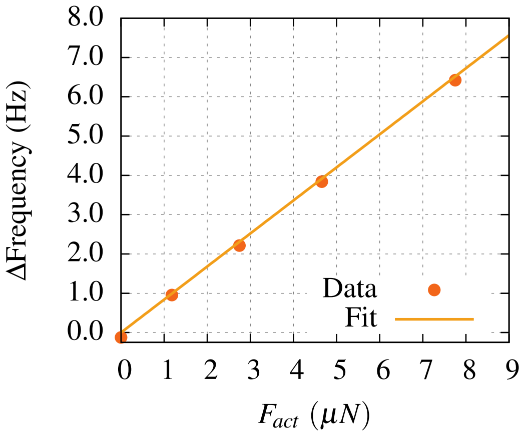

Figure 4.11: Typical result of change in resonance frequency as a function of the comb actuation voltage.

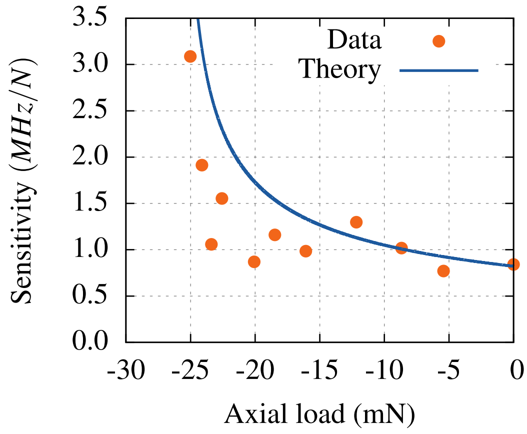

Figure 4.12: Sensitivity of the DETF resonance frequency to an actuation voltage on the actuation combs.

Using the comb actuators connected to the roller block, small forces were exerted on the DETF as well. Measurement data for no applied axial load is shown in figure 4.11. The actuation force was determined through equation 3.1 and is corrected for the high lever stiffness. The sensitivity of the DETF at this load can be found by determining the slope of the graph. Data for each applied axial load separately looks very similar to that in figure 4.11. However, when all data for different axial loads is compared like in figure 4.12, the consistency between the data points is not too good. Closer inspection of the measurements revealed a noticeable upward drift of the DETF resonance frequency still long after the vacuum of the system had settled. Because the sensitivities in figure 4.12 are determined through frequency shifts of only a few Hertz and the measurements taken by the gain-phase analyzer take quite some time, this drift significantly influences the measurement results. What exactly causes this upward drift is unknown, but it seems to be a stabilization effect with a large time constant, because the drift velocity diminishes over time. Fact is that the measurements in figure 4.12 were conducted before equilibrium was reached and therefore show a large amount of scatter. Unfortunately, redoing the measurements on this structure is not possible because of the one directional nature of the ratchet structure.

4.2.4 Stability

For accurate measurements, not only the transducer's sensitivity, but also its stability is important. To get insight in the limits on stability of a DETF, the resonance frequency of an unloaded DETF was monitored for an hour. In this period, the resonance frequency was sampled twice per second by measuring the DETF output phase at a constant driving frequency around resonance. Fluctuations in this phase can be directly related to fluctuations in the frequency. It would be interesting to sample the resonance frequency at a much higher rate. This way, the fundamental limitation in resolution by resonator phase noise can be observed [8]. Unfortunately, this setup only allows for slow sampling and only the long term stability can be investigated.

In figure 4.13, the monitored resonance frequency over a one hour period is shown. Neglecting the two spikes, the maximum absolute shift is approximately $0.1Hz$. The largest change in frequency happens very slow and is probably caused by frequency drift. These slow effects can be easily filtered out, also when the DETF is operated in a sensor. In the frequency band $0.1-1Hz$, the noise level is below $5mHz/\sqrt{Hz}$. Combined with the measured sensitivities from figure 4.12, this gives a noise level of $2-5nN$ for signal frequencies in the range $0.1-1Hz$. For frequencies above $1Hz$, another setup is needed to measure the stability.

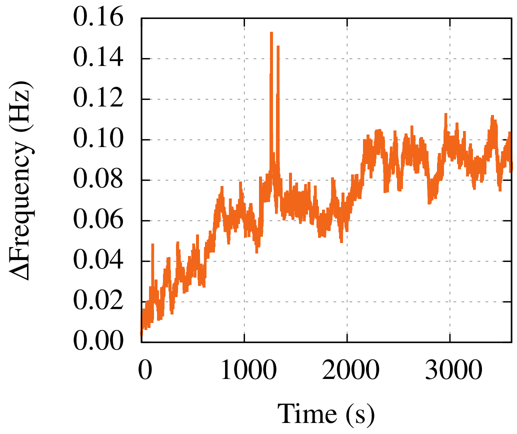

Figure 4.13: DETF resonance frequency shift over a one hour period. Sample rate is 2Hz.

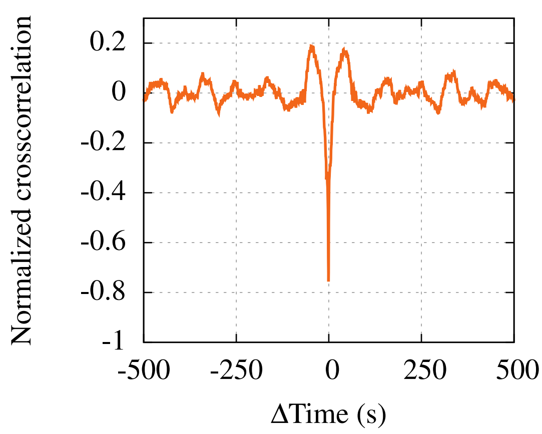

Figure 4.14: Cross correlation of DETF resonance frequency and the readout bias voltage, V_b.

While collecting the data in figure 4.13, the bias voltage was accurately measured as well. It turns out that the two signals are highly correlated and that much of the frequency shift occurring in the DETF is caused by a slight change in the bias voltage on the readout electrodes. In figure 4.14, the normalized cross correlation between the resonance frequency and the bias voltage is shown. This plot shows that for zero time lag, the signals are highly correlated, indicating that much is to be gained in improving the stability of the bias voltage. The measured noise from the used Delta supply is approximately $150\mu V/\sqrt{Hz}$ on a bias voltage of $12V$.

4.2.5 Nonlinear response

As was discussed in section 2.4, the DETF will show nonlinear behavior for large driving amplitudes. The resonance frequency will be a function of the oscillation amplitude and the transfer will show hysteresis. Recall from section 2.4 that the nonlinear oscillation frequency is given by

$$\omega_0' = \omega_0(1+\frac{3c_2}{8c_0}y_0^2) \qquad \text{with:} \quad c_0 = \frac{192EI}{L_t^3} - \frac{4V_b^2 L_r t\varepsilon_0}{g^3}, \quad c_2 = \frac{147.3EI}{L_t^3 w_t^2} - \frac{24V_b^2 L_r t\varepsilon_0}{g^5} \tag{4.4}$$

where y_0 is the oscillation amplitude. The change in resonance frequency is dependent on the bias voltage mainly through c_2. When the bias voltage is relatively low, the first term in c_2 is dominant, c_2 will be positive and the resonance frequency will increase with large vibration amplitudes. This effect is shown in figure 4.15. Transfer functions were measured at $V_b = 15V$ at varying driving levels. Hysteresis effects are clearly visible for the larger driving levels and the resonance frequency is clearly going up with increasing oscillation amplitude. This indicates that at a $15V$ bias, c_2 is positive and the mechanical spring hardening is still dominant. The same measurements were repeated at $30V$ bias. These results are shown in figure 4.16. Here the results are similar, but the resonance frequency goes down with increasing oscillation amplitude. At this bias, c_2 has become negative and is dominated by the nonlinearity in the capacitive readout. At a specific bias voltage somewhere between $15V$ and $30V$, the second order nonlinearity is equal to zero and the system is linear up to third order correction terms. This means that the vibration amplitude can be increased further without hysteresis occurring. This range is consistent with the estimation in equation 4.4. Filling in the specific values the DETF geometry, c_2 vanishes at $V_b \approx 21V$. It would be interesting to investigate further how well this technique works for avoiding hysteresis and at which amplitude higher order nonlinearity starts limiting the oscillation amplitude.

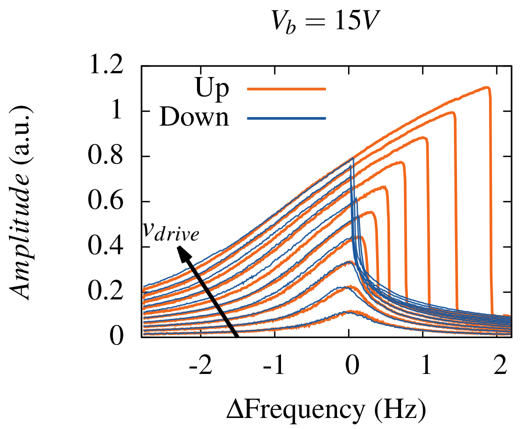

Figure 4.15: Transfers measured at a bias of $15V$ for increasing driving amplitudes. The resonance frequency shifts up for higher driving amplitudes.

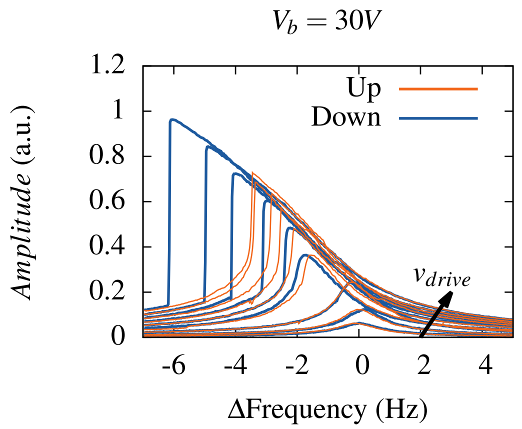

Figure 4.16: Transfers measured at a bias of $30V$ for increasing driving amplitudes. The resonance frequency shifts down for higher driving amplitudes

The amplitudes in figures 4.15 and 4.16 are given in arbitraty units. The scale is equal for both figures, so they can be compared with each other. That is useful, but to extract absolute information on the value of the c_2 for example, it would be nice to have the absolute amplitudes available. However, determining the absolute vibration amplitude is very difficult, because they are extremely small, in the order of tens of nanometers. It could be done by overdriving the DETF far into the nonlinear region and optically measuring the DETF displacement to calibrate the readout system. This, however, is subject for further study.

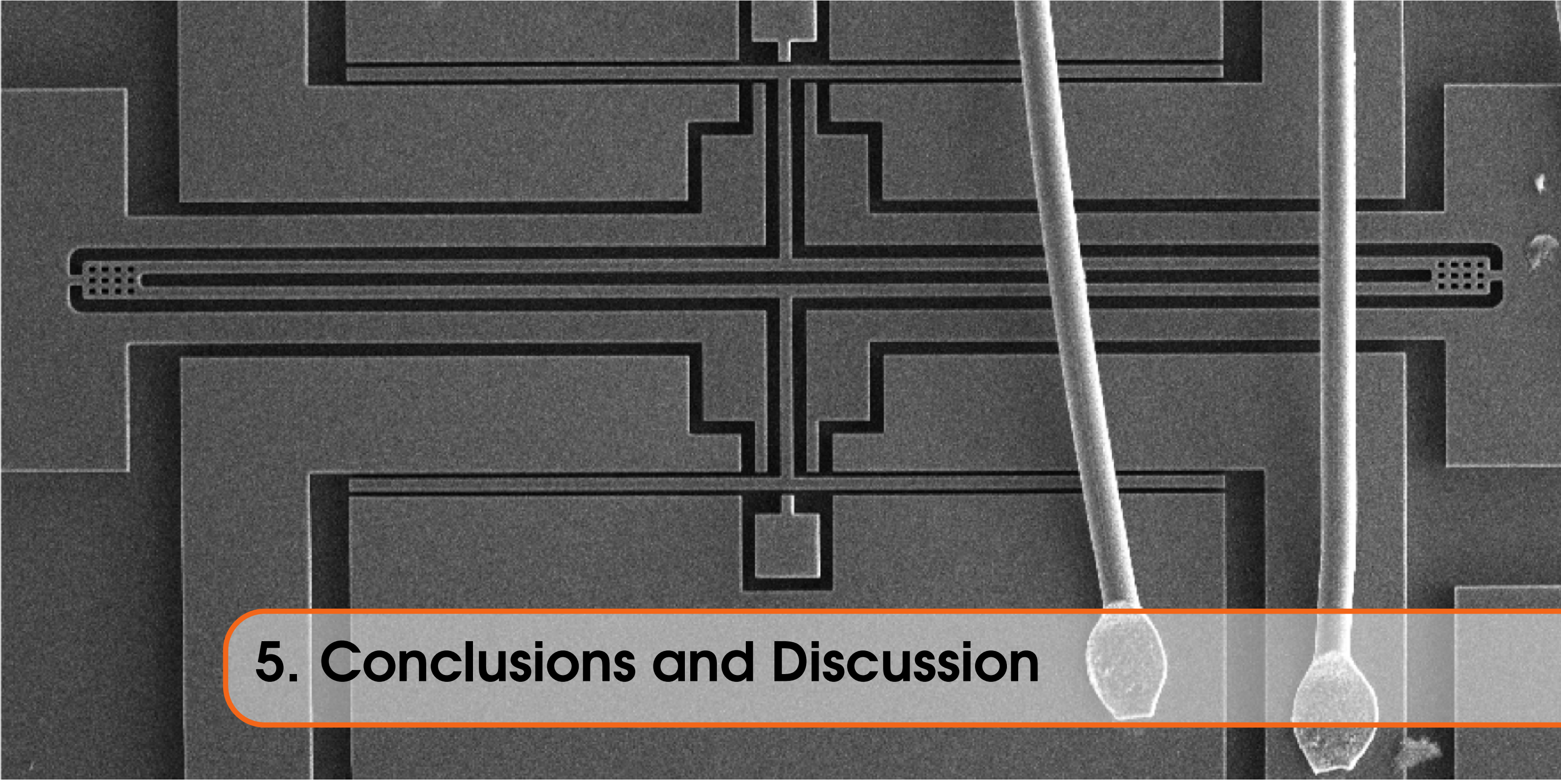

5. Conclusions and Discussion

5.1 Conclusion

The designed MEMS device for loading the DETF structure worked well and gave a lot of insight in the behavior of double ended tuning fork structures. The quality factor of the system can be made very high by lowering the pressure in the system below 10^{-2}mbar. A reliable way was established to measure the mechanical quality factor of the DETF through the electronic interface, without the need to perform a ringdown measurement. This method can also be used in other high quality factor systems where damping in the electronics influences the measurements. The mechanical quality factor of an unloaded DETF was found to be $98.7 \cdot 10^3 \pm 2.7 \cdot 10^3$, which is comparable to the highest quality factors reported for similar structures.

When applying axial loads to the structure, the DETF buckles somewhat earlier than the model predicts. This is expected, because by actuating the structure, it is pulled out of its equilibrium situation. The structure can be loaded to about 95% of the predicted buckling load before it actually buckles. Loading the structure with a large preload theoretically increases the sensitivity of the DETF structure to small loads. For a preload that is 90% of the predicted buckling load, this sensitivity should be about 3.2 times larger than with no preload. Unfortunately, no conclusive measurements could be done yet, because of an unexplained drift in the system.

The stability of the system could only be measured up to $1Hz$. In this band, the system is dominated by slow temperature drift below $100mHz$. Because no interesting signals will be at such low frequency, this can be filtered out quite easily. Between $0.1Hz$ and $1Hz$, the frequency stability of an unloaded DETF is below $5mHz/\sqrt{Hz}$. This can probably be significantly improved by using a more stable voltage source for biasing the readout structure. The frequency instability was found to be highly correlated to the bias voltage. The frequency stability of the unloaded DETF provides a lower limit for the DETF, as loading it seems to have a negative effect on the stability. When the springs are compressed and a large axial load is applied to the DETF, the resonance frequency starts drifting and takes a very long time to settle. What exactly causes this drift is still unknown. For quickly varying signals, the resolution of the DETF is limited by resonator noise. Using this measurement setup, however, this cannot be quantified.

Measured sensitivities of the DETF structure under test, vary between about $1-3MHz/N$, depending on the applied axial load. Combined with the lower limit of the stability at $5mHz/\sqrt{Hz}$, this gives a noise floor of $2-5nN$ for slowly varying signals. This is good for a very sensitive force sensor, but it is not good enough for use in an ultra sensitive MEMS accelerometer. Even when using a ridiculously large mass of $100mg$, the noise floor would still be around $1\mu g$, about 1000 times too large. A lot of things can still be improved in this structure, but decreasing the noise with a factor 1000 might not be realistic.

The mechanical spring hardening effect introduces nonlinearities in the system and this limits the allowed vibration amplitude of the system. Measurements indicate that the spring hardening effect can be compensated by a spring softening effect introduces by the capacitive readout system. By carefully choosing the readout bias voltage, the allowed vibration amplitude will increase. A large vibration amplitude could improve the mechanical signal to noise ratio and this is beneficial of the achievable resolution.

5.2 Discussion

Most parts of the designed MEMS device worked properly, with the exception of one important structure: the thermal actuator. The dimensions of this actuator structure were taken from another design where the actuator was used to compress a spring of similar spring constant as in the design in this work. The big difference was the amount of springs in the ratchet structure. Scaling down devices means that surface effects like contact friction become increasingly more dominant. Adding multiple springs in the ratchet was a good idea to improve the step resolution, but also adds a lot of contact area that produces friction forces as they slide along the ratchet teeth. In the end this meant that the thermal actuator was not strong enough to compress the ratchet structure. Luckily, the ratchet was designed in such a way that it could also be operated using a probe needle. However, manually manipulating MEMS devices with an accuracy below $10\mu m$ is very error prone and many devices got stuck during this process. This, combined with the one-directional nature of the ratchet structure is the reason that the sensitivity measurements that were influenced by the frequency drift in the system, could not be easily redone.

The DETF structures that are considered in this work are actuated and monitored through parallel plate capacitor structures. In the fabricated MEMS device, DETF's with a comb-like readout structure were also incorporated, because capacitive combs have a more linear behavior. Because too much time went in managing to properly apply a load to the DETF structures, this alternative readout system was not investigated further. It would still be interesting to compare the two different readout and actuation systems in terms of efficiency and linearity, though.

A major property of a DETF resonator that has not been properly treated in this work is the noise in the frequency output. For quickly varying signals, it is impossible to determine the resonance frequency by averaging many periods, and the resolution is limited by this frequency noise. Extensive theory exists to predict and describe this noise, and it would be good to investigate this effect and quantify the amount of noise in the system. To do this, a fully different measurement setup is needed. A stable oscillating circuit has to be implemented, such that the resonance frequency can be tracked in real-time. As the electronics were not the focus here, this subject remains unattended, but for a complete view of the DETF behavior, it is an important point that still needs to be addressed.

Having an oscillator circuit to track the DETF resonance frequency in real-time also provides to opportunity to remove the effects of drift on the sensitivity measurements to large extent. Instead of taking minutes, such a measurement could be finished within seconds, giving the DETF no time to drift significantly.

Another point that has to be investigated further is the dependence of the quality factor on the axial load. The measured quality factors in this work were taken with no applied axial load. At very large axial loads however, the quality factor seemed to drop significantly. For determining whether it is beneficial to preload a DETF to increase its sensitivity, it is important to know whether the quality factor remains high enough. A lower quality factor means a higher noise floor, and this could destroy the benefits of having a higher sensitivity. Due to the one-way nature of the ratchet, this effect could not be checked further on this device and is a subject for future study.

In general, the signal to noise ratio of a DETF is limited by nonlinear effects, because they severely limit the allowed drive amplitude. The nonlinear behavior of the system as a whole shows some interesting effects that could stretch this limit. An analysis that is supported by the measurements indicates that the second order nonlinearity can be entirely removed by carefully choosing the system bias voltage. It would be good to further study this subject. More measurements can be easily performed to see how much the vibration amplitude can be increased before a higher order nonlinearity becomes the limiting factor. Higher order nonlinearities can also be included in the model to check this limit.

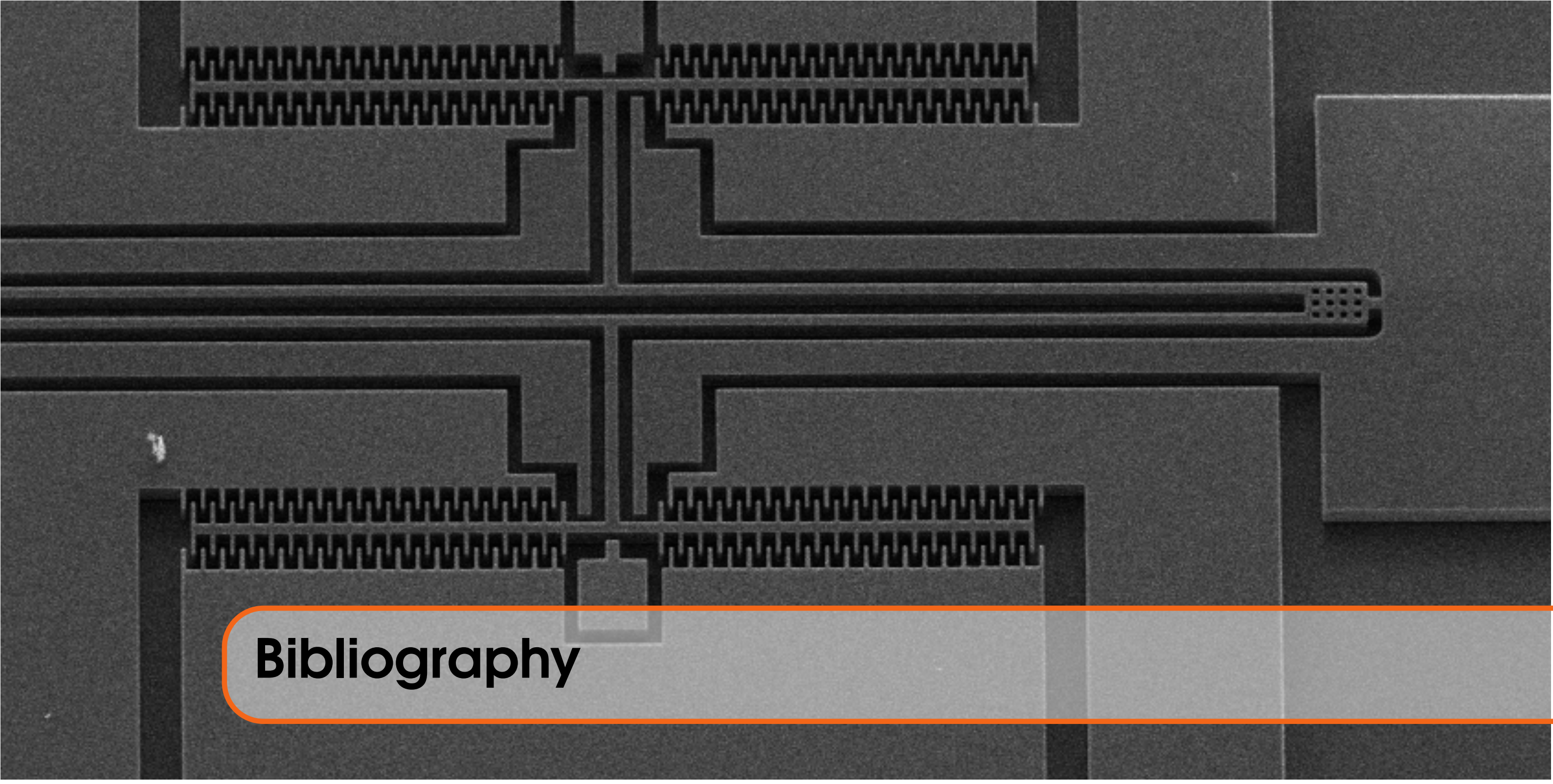

Bibliography

Books

[5] M. Bao. *Analysis and Design Principles of MEMS Devices*. Elsevier Science, 2005. ISBN: 9780080455624 (cited on page 22).

[6] S. Beeby. *MEMS Mechanical Sensors*. Artech House microelectromechanical systems (MEMS) series. Artech House, 2004. ISBN: 9781580538732 (cited on page 17).

[9] M. Elwenspoek and R.J. Wiegerink. *Mechanical Microsensors*. Microtechnology and MEMS. Springer, 2001. ISBN: 9783540675822 (cited on pages 15, 28, 46).

[13] G. Krijnen M. Elwenspoek and R. Wiegerink. *Introduction to Mechanics and Transducer Science*. University of Twente, 2008 (cited on pages 10, 12).

[15] H.M.J.R. Soemers. *Design Principles: For Precision Mechanisms*. Herman Soemers, 2011. ISBN: 9789036531030 (cited on pages 13, 23–25).

[17] S.T. Thornton and J.B. Marion. *Classical Dynamics of Particles and Systems*. Brooks/Cole, 2004. ISBN: 9780534408961 (cited on page 45).

[18] W. Weaver, S.P. Timoshenko, and D.H. Young. *Vibration Problems in Engineering*. A Wiley-Interscience publication. John Wiley & Sons, 1990. ISBN: 9780471632283 (cited on pages 12, 44, 45).

Articles

[1] T Accadia et al. “Virgo: a laser interferometer to detect gravitational waves”. In: *Journal of Instrumentation* 7.03 (2012), P03012 (cited on page 7).

[2] F Acernese et al. “Advanced Virgo: a second-generation interferometric gravitational wave detector”. In: *Classical and Quantum Gravity* 32.2 (2015), page 024001 (cited on page 7).

[3] K. Azgin, T. Akin, and L. Valdevit. "Ultrahigh-Dynamic-Range Resonant MEMS Load Cells for Micromechanical Test Frames". In: *Microelectromechanical Systems, Journal of* 21.6 (Dec. 2012), pages 1519–1529. ISSN: 1057-7157. DOI: 10.1109/JMEMS.2012.2211576 (cited on pages 8, 12, 20).

[7] R.N. Candler et al. "Impact of geometry on thermoelastic dissipation in micromechanical resonant beams". In: *Microelectromechanical Systems, Journal of* 15.4 (Aug. 2006), pages 927–934. ISSN: 1057-7157. DOI: 10.1109/JMEMS.2006.879374 (cited on page 30).

[8] AN Cleland and ML Roukes. "Noise processes in nanomechanical resonators". In: *Journal of Applied Physics* 92.5 (2002), pages 2758–2769 (cited on pages 15, 33).

[10] M.A. Hopcroft, W.D. Nix, and T.W. Kenny. "What is the Young's Modulus of Silicon?" In: *Microelectromechanical Systems, Journal of* 19.2 (Apr. 2010), pages 229–238. ISSN: 1057-7157. DOI: 10.1109/JMEMS.2009.2039697 (cited on page 44).

[12] V. Kaajakari et al. "Nonlinear limits for single-crystal silicon microresonators". In: *Microelectromechanical Systems, Journal of* 13.5 (Oct. 2004), pages 715–724. ISSN: 1057-7157. DOI: 10.1109/JMEMS.2004.835771 (cited on pages 15–17).

[16] G Stemme. "Resonant silicon sensors". In: *Journal of Micromechanics and Microengineering* 1.2 (1991), page 113 (cited on page 20).

[19] M. Weinberg et al. "Energy loss in MEMS resonators and the impact on inertial and RF devices". In: (June 2009), pages 688–695. DOI: 10.1109/SENSOR.2009.5285418 (cited on page 29).

Miscellaneous

[4] N.A. van Bakel. *Silent sensors for stellar echo's and seismic surveys*. June 2013 (cited on page 7).

[11] V. Kaajakari. *Nonlinearity in Micromechanical Resonators* (cited on pages 16, 17).

[14] B. John Merchant. *MEMS Applications in Seismology*. Nov. 2009 (cited on page 8).

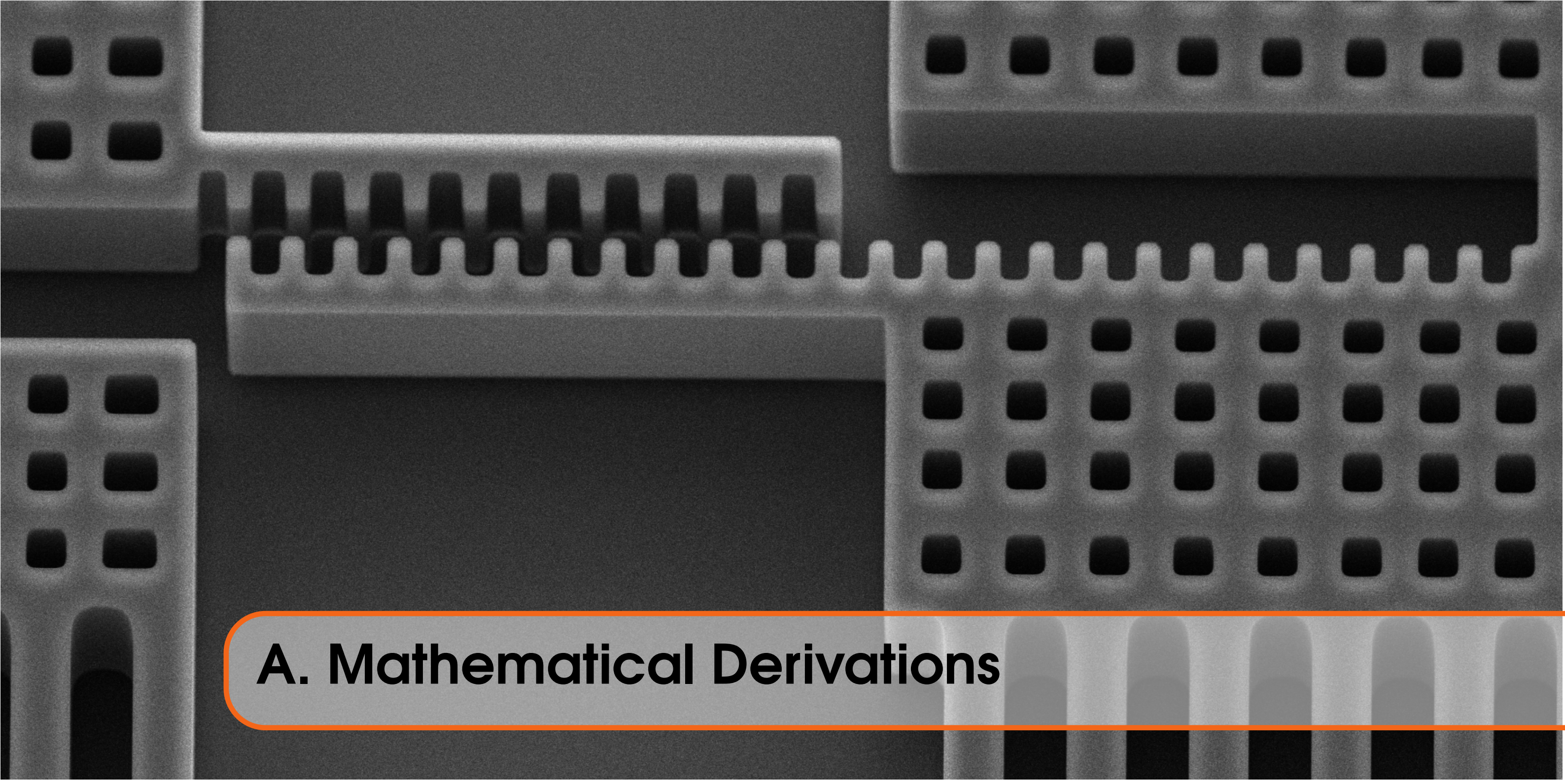

A. Mathematical Derivations

A.1 Prismatic springs

Throughout this work, a lot of springs are used that consist of prismatic beams of constant cross section that are clamped at both sides. The spring constants and their deflection shapes play an important role in multiple parts of the MEMS design. These subjects will therefore be investigated here.

A.1.1 Deflection shape

In figure A.1 an illustration of a prismatic beam with relevant boundary conditions is shown. At $x = 0$, the beam is clamped. At $x = \ell$, the beam is guided, which means that only displacement in the y-direction is possible and no rotation can occur. Moreover, a force F loads the beam at $x = \ell$.

The relationship between the beam's deflection shape $v(x)$ and an applied load can be described by the Euler-Bernoulli equation in relation A.1. In the case depicted in figure A.1, the force per unit length, $f(x)$, can be represented mathematically by a delta function,

$$f(x) = \delta(x - \ell)F. \tag{A.1}$$

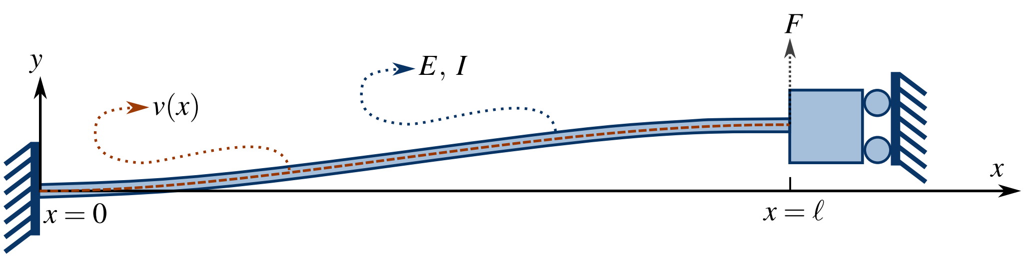

Figure A.1: Illustration of a prismatic clamped-guided beam with Young's Modulus E and area moment of inertia I, that can be used as a spring element. At $x = 0$ the beam is clamped and displacement and rotation are inhibited. At $x = \ell$, the beam is guided and therefore rotation is inhibited. Under load F and these boundary conditions, the beam adjusts to a specific shape, $v(x)$.

Relation A.1 — Euler-Bernoulli. The relationship between a static deflection $v(x)$ of a narrow beam and a load per unit length, $f(x)$, is described by the Euler-Bernoulli equation [18, p. 331]:

$$\frac{d^2}{dx^2}\left(EI\frac{d^2v(x)}{dx^2}\right) = -f(x), \tag{A.2}$$

where E is the Young's modulus of the beam material and I is its area moment of inertia.

For a beam with a constant cross section, the area moment of inertia, I, remains a constant along the length of the beam and equation A.2 can be rewritten as

$$\frac{d^4v(x)}{dx^4} = -\frac{f(x)}{EI} = -\delta(x-\ell)\frac{F}{EI}. \tag{A.3}$$

Simply integrating this result four times gives a result for the deflected shape of the beam as

$$v(x) = -\frac{Fx^3}{6EI} + \frac{C_1x^2}{2} + C_2x + C_3, \tag{A.4}$$

in which C_n are arbitary integration constants. These integration constants can be determined by taking into account the boundary conditions on the beam. In this case there are three distinct boundary conditions, being

$$v(0) = 0, \tag{A.5}$$

$$\left.\frac{dv}{dx}\right|_{x=0} = 0 \quad \text{and} \tag{A.6}$$

$$\left.\frac{dv}{dx}\right|_{x=\ell} = 0. \tag{A.7}$$

From conditions A.5 and A.6 follows that C_3 and C_2 must be equal to zero. C_1 can be determined from the third condition, A.7. Differentiation of $v(x)$ and filling in $x = \ell$ gives

$$-\frac{F\ell^2}{2EI} + C_1\ell = 0 \qquad \Rightarrow \qquad C_1 = \frac{F\ell}{2EI}. \tag{A.8}$$

Using these values for the constants C_n, this means that the deflected shape of the loaded beam with these boundary conditions can be written as

$$v(x) = -\frac{Fx^3}{6EI} + \frac{F\ell x^2}{4EI} = \frac{F\ell^3}{12EI}\left(3\left(\frac{x}{\ell}\right)^2 - 2\left(\frac{x}{\ell}\right)^3\right). \tag{A.9}$$

A.1.2 Spring constant

The spring constant of such a beam can be derived from the deflected shape in equation A.9. The displacement at the loaded end is given by $v(\ell)$. The force is known, so the spring constant is

$$c_{bend} = \frac{F}{v(\ell)} = \frac{12EI}{\ell^3}. \tag{A.10}$$

A prismatic beam can also be loaded axially. In such a case, the spring constant is given by

$$c_{axial} = \frac{EA}{\ell}, \tag{A.11}$$

where A is the beam's cross section. Since silicon is an anisotropic material, its Young's modulus can in general not be expressed as a single value, but is dependent on the crystal orientation along which strain occurs. Luckily, because of the orthogonal nature of the design, all main strain directions are aligned with the $< 110 >$ crystal orientation. This justifies the use of the Young's modulus as a single value of $169GPa$ [10].

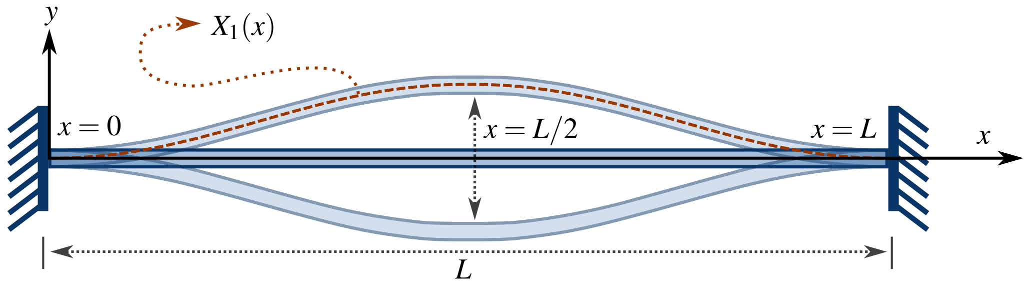

Figure A.2: Illustration of the fundamental mode of a prismatic beam with constant cross section and length L. The beam periodically moves back and forth between the two shown extrema, while the mode shape does not change. The mode shape is described by equation A.14. Maximum displacement occurs at $x = L/2$.

A.2 Resonant frequency of axially unloaded beams

To arrive at an expression for the resonant frequency of an axially unloaded beam, first the concept of Lagrangian dynamics is introduced. Then, the concept of mode shapes is illustrated. Using these theories, the resonance frequency of a prismatic beam can be expressed including the effect of geometry, axial load and capacitive readout.

A.2.1 Lagrangian dynamics

For deriving the relations for the resonant frequency of an axially loaded beam, the principle of Lagrangian dynamics is used [17, Ch. 7]. This method uses an analysis of the internal energy in a system. Two types of internal energy are distinguished: potential (U) and kinetic (T) energy. The so called Lagrangian of the system is the difference between the two energies, $\mathscr{L} = T - U$. The differential equation governing the system dynamics can be found as described in Theorem A.2.1. This means that once the internal energy of a system is known, the resonance frequency can be determined through equation A.12.

Theorem A.2.1 — Lagrangian Dynamics. A system with a Lagrangian function, $\mathscr{L}(q, \dot{q}, t)$, that depends on a generalized coordinate, q, its temporal derivative, $\dot{q}$, and the time, t, will be governed by the Euler-Lagrange differential equation [17, Ch. 7]:

$$\frac{\partial \mathscr{L}}{\partial q} - \frac{d}{dt}\frac{\partial \mathscr{L}}{\partial \dot{q}} = 0 \tag{A.12}$$

A.2.2 Mode shapes

In general, the shape, $v(x,t)$, of a vibrating beam is a function of time, t, and the position along the beam, x. In the special case of a stationary vibration, these variables can be separated and the shape can be described as [18, p. 309]

$$v(x,t) = q(t) \cdot X(x), \tag{A.13}$$

where $q(t)$ is a continuous, periodic function of t and $X(x)$ is the so called mode shape of the vibration. When the mode shape of the vibration is known, all internal energies can be obtained as a function of $q(t)$ and $\dot{q}(t)$ and the resonant frequency can be determined by solving equation A.12. Finding the exact modeshape for the DETF is hard, but luckily there are some limiting cases of which the mode shapes are known.

One of the limiting cases is a prismatic beam of constant cross section such as the one shown in figure A.2. Because the mass density is not a function of x, relatively simple analytical mode

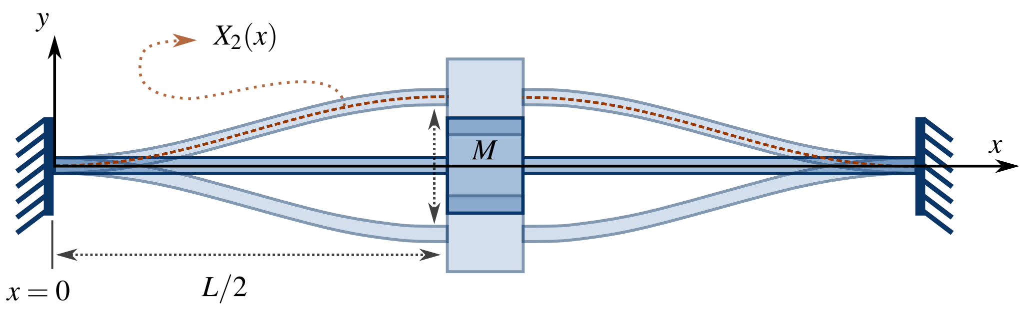

Figure A.3: Illustration of the fundamental vibration mode of a large mass suspended by prismatic beams. The beam periodically moves back and forth between the two shown extrema, while the mode shape does not change. The mode shape is described by equation A.15. Maximum displacement occurs at the center.

shapes can be derived [9, p. 212]. The analytical form of the fundamental mode shape of such a beam is described in relation A.2.

Relation A.2 — Mode shape for a prismatic beam. The mode shape, $X_1(x)$, of a vibrating prismatic beam with constant cross section and length, L, is given by [9, p. 212]:

$$X_1(x) = \cosh\left(\frac{kx}{L}\right) - \cos\left(\frac{kx}{L}\right) + \eta\left(\sin\left(\frac{kx}{L}\right) - \sinh\left(\frac{kx}{L}\right)\right). \tag{A.14}$$

with:

$k \approx 4.730$

$$\eta = \frac{\cosh k - \cos k}{\sinh k - \sin k}$$

A second limiting case occurs when all mass is concentrated at the center of a prismatic beam. Practically, this happens when a large mass is suspended by prismatic beams. The beams now are purely spring elements and their mass can be neglected. This situation is illustrated in figure A.3. Because in this case the mass of the beams is negligible, they are not subject to any inertial forces. The shape of the springs can therefore be described by the static deflected shape of a prismatic beam. Equation A.9 represents this statically deflected shape. Noting that the length of the beam, ℓ, is now $L/2$ and dropping all constants, the mode shape will be as described in relation A.3

Relation A.3 — Mode shape for suspended mass. The mode shape, $X_2(x)$, of a large mass suspended by prismatic beams of constant cross section as shown in figure A.3 is equal to the static deflection curve of a clamped-guided prismatic beam. For $0 < x < L/2$, this mode shape can be described by

$$X_2(x) = 12\left(\frac{x}{L}\right)^2 - 16\left(\frac{x}{L}\right)^3. \tag{A.15}$$

The mode shape is symmetrical in $x = L/2$.

Both mode shapes are described by very different functions, but they actually are quite similar. In figure A.4, both $X_1(x)$ and $X_2(x)$ are plotted, normalized to their maximum values. As can be seen in the plot, differences between both mode shapes are quite small. The results obtained for the resonant frequency of the system using either of the two shapes is therefore expected to be small as well. A comparison is made in section A.2.4.

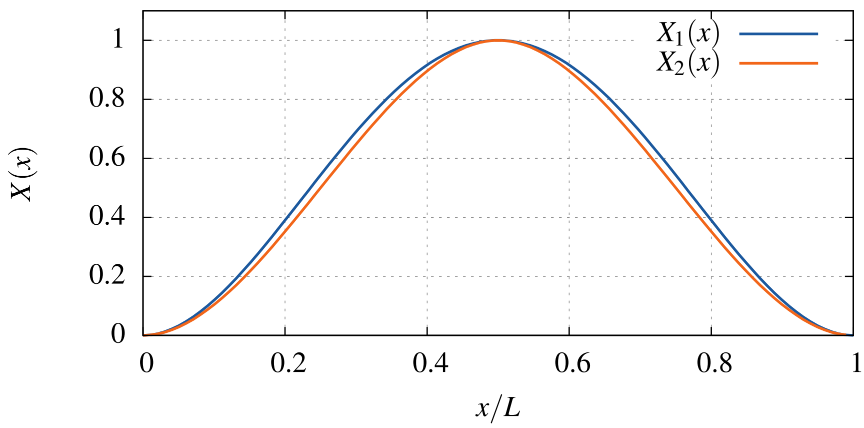

Figure A.4: A plot of both the fundamental mode shape of a prismatic beam with constant cross section, $X_1(x)$, and of a large suspended mass suspended by prismatic beams, $X_2(x)$.

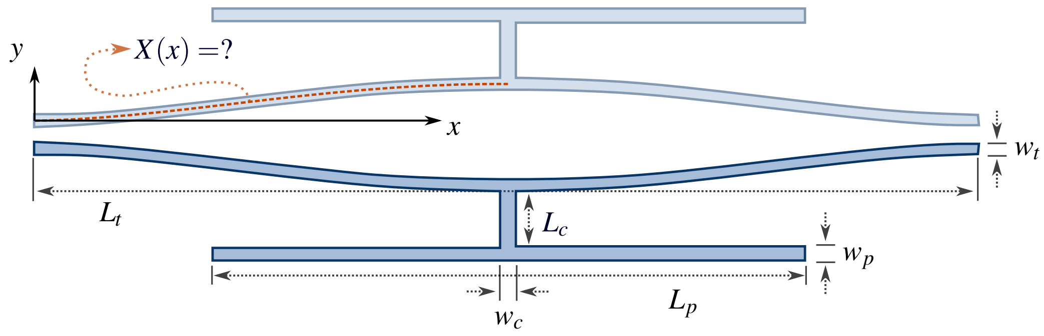

Figure A.5: An illustration of one of the extremes of the vibrating DETF structure. Both tines are actuated in opposite directions to cancel nett forces and moments on the anchors. The exact modeshape is unknown but will be approximated by $X_1(x)$.

A.2.3 Unloaded resonance frequency

A schematic representation of the vibrating DETF structure is shown in figure A.5. The DETF structure behaves like a system somewhere between the two limiting cases discussed before. A mass is attached to the center of the prismatic beam, but it is not so large that the mass of the beam itself can be fully neglected in determining the mode shape. Therefore, both of the extrema are compared and the difference is inspected.

The potential energy, U, in this system is determined only by the spring energy stored in the bending beam. This energy can be determined by integrating the bending energy along the beam,

$$U = \int_0^{L_t} \frac{EI}{2} \left(\frac{\partial^2 y(x,t)}{dx^2} \right)^2 dx, \tag{A.16}$$

where E is the silicon Young's Modulus and I is the beam's area moment of inertia, $I = tw_t^3/12$. Note that I is constant along the length of the beam and can be extracted from the integral. Inserting the steady state solution of equation A.13, the potential energy becomes

$$U = \frac{EI}{2} \int_0^{L_t} \left(\frac{\partial^2 (X(x)q(t))}{\partial x^2} \right)^2 dx = \frac{EI}{2} q(t)^2 \int_0^{L_t} \left(\frac{\partial^2 X(x)}{\partial x^2} \right)^2 dx = \frac{EI}{2} q(t)^2 \cdot C_1, \tag{A.17}$$

where C_1 is the constant evaluation of the integral over a given mode shape.

The kinetic energy can be found through similar reasoning. In this case the integral to be evaluated is

$$T = \int_0^{L_t} \frac{1}{2}\lambda \left(\frac{\partial y(x,t)}{dt}\right)^2 dx, \tag{A.18}$$

where λ is the mass density per unit length. The total mass attached to the center of the DETF tine is determined by the dimensions of the readout plate and is given by

$$m_c = \rho t(w_c L_c + w_p L_p), \tag{A.19}$$

where ρ is the density of the material the structure is made of. This mass, along with the constant mass density along the beam gives the mass density per unit length,

$$\lambda = \rho t w_t + \delta\left(\frac{x}{L} - \frac{1}{2}\right) m_c, \tag{A.20}$$

where $\delta(x/L - 1/2)$ is the dirac-delta function, a way of writing that the mass m_c is attached at $x = L/2$. Using this mass density and the steady state solution from equation A.13, the kinetic energy can be written as

$$T = \int_0^{L_t} \frac{\lambda}{2}\left(\frac{\partial(X(x)q(t))}{\partial t}\right)^2 dx = \frac{1}{2}\dot{q}(t)^2\left(\rho t w_t \int_0^{L_t} X(x)^2 dx + m_c\left(X\left(\frac{L}{2}\right)\right)^2\right) \tag{A.21}$$

$$= \frac{1}{2}\dot{q}(t)^2 \cdot C_2 \tag{A.22}$$

where C_2 is the constant evaluation of the integral for a given mode shape.

Using these results for the internal energy of the system, the Lagrangian of the system becomes

$$\mathscr{L} = T - U = \frac{1}{2}C_2 \cdot \dot{q}(t)^2 - \frac{EI}{2}C_1 \cdot q(t)^2. \tag{A.23}$$

Theorem A.2.1 states that the differential equation governing system dynamics then is given by

$$-EIC_1 q(t) - C_2\ddot{q}(t) = 0 \quad \Rightarrow \quad \ddot{q}(t) = -\frac{EIC_1}{C_2}q(t) \tag{A.24}$$

This is a standard second order differential equation in $q(t)$ that has the solution

$$q(t) = A\cos\left(\sqrt{\frac{EIC_1}{C_2}}t\right) + B\sin\left(\sqrt{\frac{EIC_1}{C_2}}t\right). \tag{A.25}$$

The resonance frequency of the unloaded DETF can therefore be described by

$$\omega_0 = \sqrt{\frac{EIC_1}{C_2}} = \sqrt{\frac{EI\int_0^{L_t}\left(\frac{\partial^2 X(x)}{\partial x^2}\right)^2 dx}{\left(\rho t w_t \int_0^{L_t} X(x)^2 dx + m_c\left(X\left(\frac{L}{2}\right)\right)^2\right)}} \tag{A.26}$$

A.2.4 Mode shape comparison

Equation A.26 shows that the resonance frequency of an unloaded DETF can be determined when the mode shape of the vibration is known. Evaluating the integrals in equation A.26 for both the

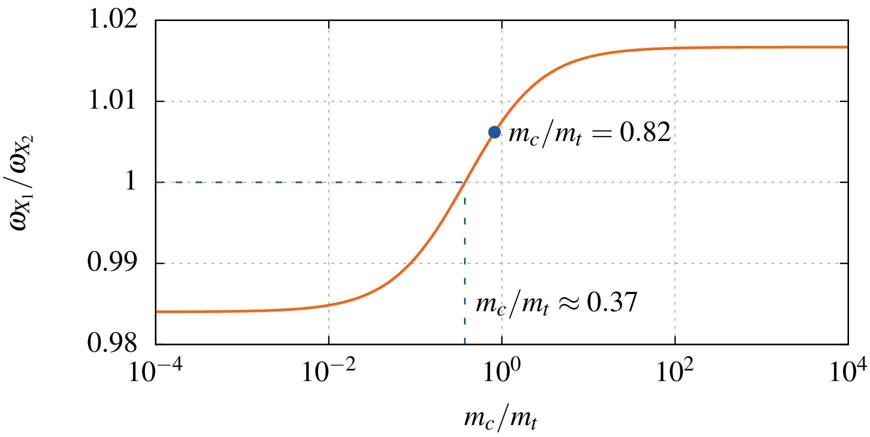

Figure A.6: The ratio of the resonance frequencies obtained by using the different mode shapes $X_1(x)$ and $X_(2)$ as a function of m_c/m_t. Both models equally overestimate the resonance frequency for $m_c/m_t \approx 0.37$. The DETF used in this work has $m_c/m_t = 0.82$.

limiting cases described in section A.2.2 results in two slightly different results for the resonance frequency,

$$\omega_{X_1} \approx \sqrt{\frac{198.46 \cdot EI}{L^3\,(0.3965 m_t + m_c)}} \quad \text{and} \tag{A.27}$$

$$\omega_{X_2} = \sqrt{\frac{192 \cdot EI}{L^3\,(\frac{13}{35} m_t + m_c)}}, \tag{A.28}$$

where $m_t = \rho t w_t L$ is the mass of a DETF tine. The ratio $\omega_{X_1}/\omega_{X_2}$ is a measure for how much the two results differ and can be written as

$$\frac{\omega_{X_1}}{\omega_{X_2}} = \sqrt{\frac{198.46 \times (\frac{13}{35} m_t + m_c)}{192 \times (0.3965 m_t + m_c)}}. \tag{A.29}$$

This ratio depends on the ratio of the mass of the DETF tine, m_t, compared to the mass that is connected to the center of the DETF tine, m_c. The ratio in equation A.29 is plotted as a function of m_c/m_t in figure A.6. A few things can be noted from this graph. For low m_c/m_t, the mass attached to the center of the DETF can be neglected and $X_1(x)$ is known to correctly describe the mode shape of the DETF. In the graph can be seen that in this case, using mode shape $X_2(x)$ will overestimate the resonance frequency by about 1.6%.

On the other hand, with very large m_c/m_t, the mass of the DETF tines can be neglected and $X_2(x)$ is known to correctly describe the DETF mode shape. In this case, using mode shape $X_1(x)$ will overestimate the resonance frequency by about 1.7%. Between these two extremes, both mode shapes will lead to a slight overestimation of the DETF resonance frequency. The overestimation will always be less than 1.7%, though, which is accurate enough to form a model.

Both models overestimate the resonance frequency by the same amount for $m_c/m_t \approx 0.37$, this is also indicated in figure A.6 as the point where $\omega_{X_1}/\omega_{X_2} = 1$. For $m_c/m_t > 0.37$, using $X_2(x)$ will give better results and for $m_c/m_t < 0.37$, using $X_1(x)$ will give better results. The DETF considered in this work has $m_c/m_t = 0.82$, a point also indicated in figure A.6. As this is bigger than 0.37, $X_2(x)$ will be used to approximate the mode shape of vibration.

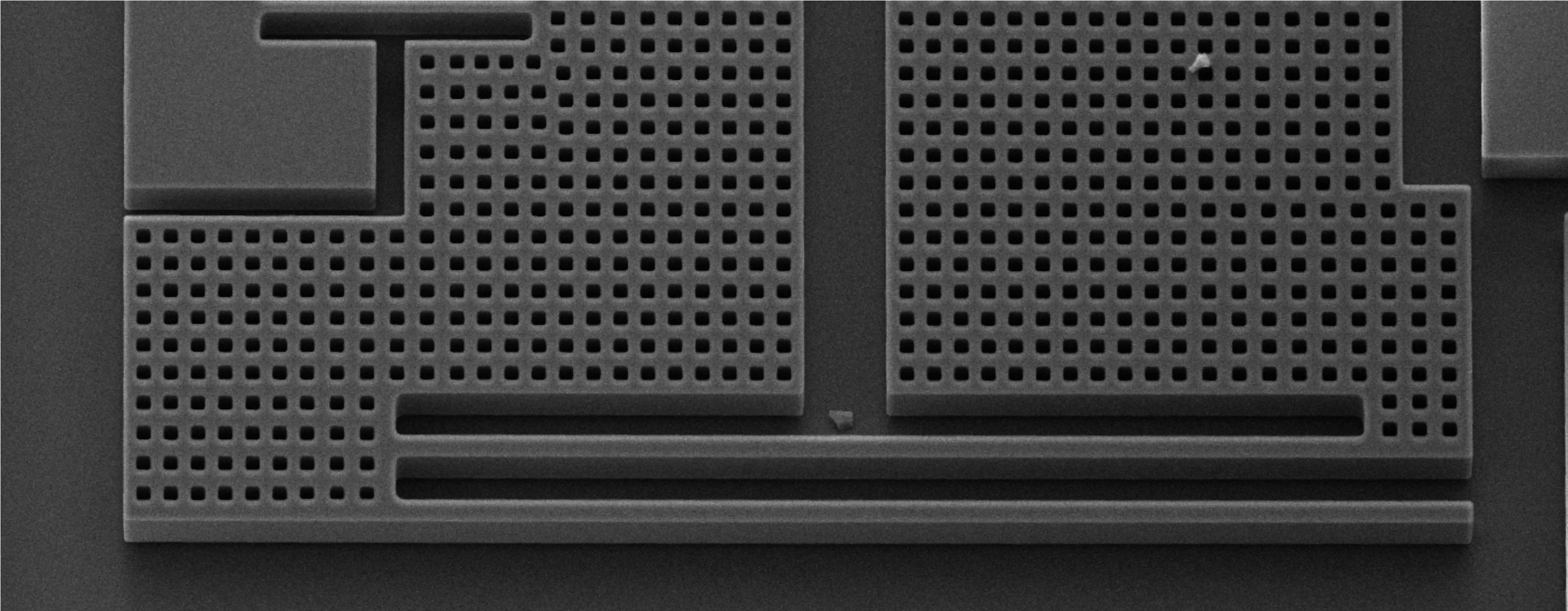

B. Production Process

• Substrate selection • SOI 25-2-400 • Orientation: h100i • Device layer: $25\mu m$, P++ • Handle layer: $400\mu m$, P+	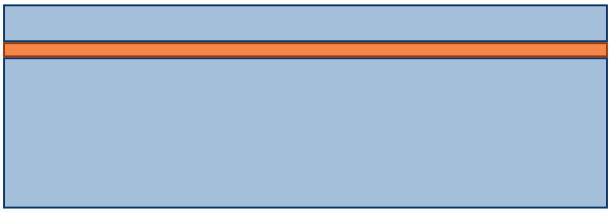
• Wafer cleaning • Wet thermal oxidation, $2\mu m$ • Temperature: $1150°C$ • Time: $12{:}00h$ • Measurement of oxide layer thickness	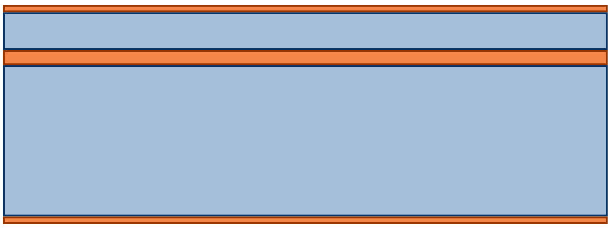
• Coating handle layer with photoresist, Olin 907-17 • Exposure, mask: HANDLE	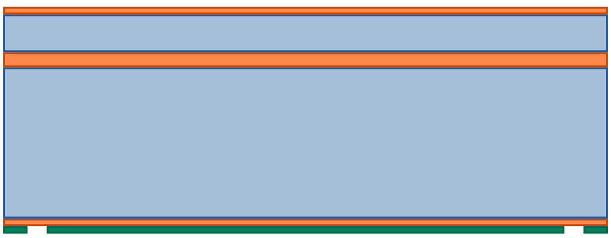

• Etching of silicon dioxide in Adixen DE • Depth: $2\mu m$ • Time: ≈ 5 min	
• Stripping resist, cleaning wafer	
• Coating device layer with photoresist, Olin 907-17 • Exposure, mask: DEVICE	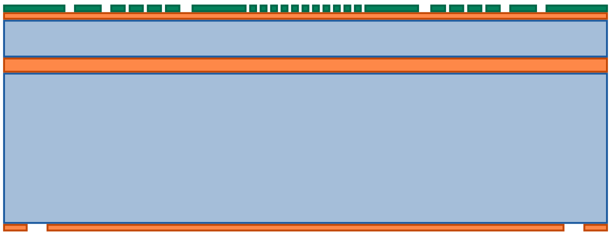
• Etching of silicon dioxide in Adixen DE • Depth: $2\mu m$ • Time: ≈ 5 min	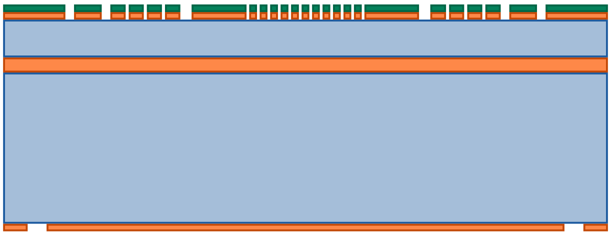
• DRIE etching of silicon in Adixen, top side • Recipe: RB.HARS • Depth: $25\mu m$ • Time: ≈ 9 min	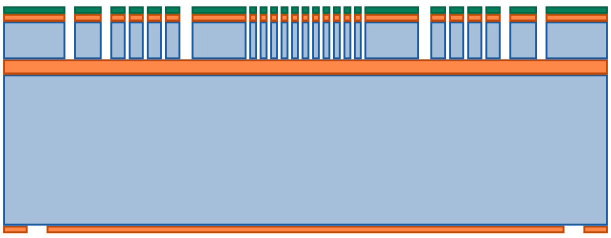

• DRIE etching of silicon in Adixen SE, bottom side • Recipe: RB.HARS • Depth: 400μm • Time: $\approx$ 36 min	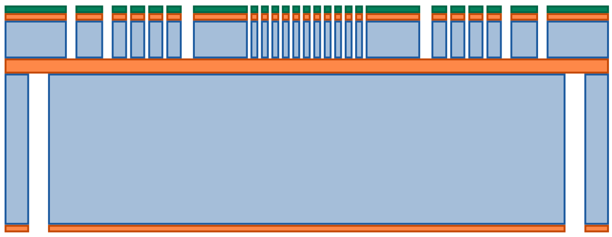
• Stripping resist, cleaning wafer • Fluor carbon removal • O_2 plasma cleaning, 800 Watt, 1 hour • Piranha cleaning, 30 min	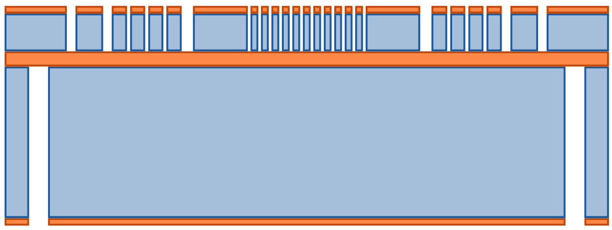
• Etching of oxide in 50% HF • Time: $\approx$ 2 min until oxide at top and bottom side is removed	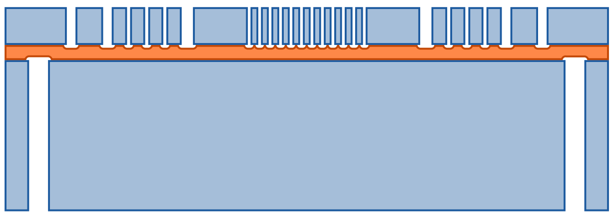
• Vapor-HF to relaease structure and devices • Time: 45 min	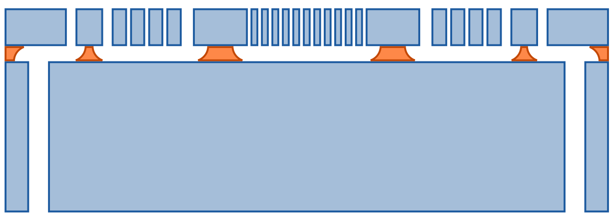
• Release samples by removing surrounding frame • Measurement/Inspection of samples